Contribution of black carbon and desert dust to aerosol absorption in the atmosphere of the Eastern Arabian Peninsula

Mohamed M.K. Mahfouz, Gregor Skok, Jean Sciare, Michael Pikridas, M. Rami Alfarra, Shamjad Moosakutty, Balint Alfoldy, Matic Ivančič, Martin Rigler, Asta Gregorič, Rok Podlipec, Svenja Lohmann, Gregor Hlawacek, Rene Heller, Ersin Tutsak, Griša Močnik

Atmospheric Environment 324 (2024) 120427

Contents lists available at ScienceDirect

Atmospheric Environment

journal homepage: www.elsevier.com/locate/atmosenv

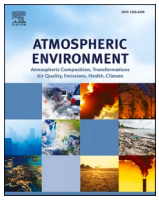

Contribution of black carbon and desert dust to aerosol absorption in the atmosphere of the Eastern Arabian Peninsula

Mohamed M.K. Mahfouz [a,b,*], Gregor Skok [b], Jean Sciare [c], Michael Pikridas [c], M. Rami Alfarra [d], Shamjad Moosakutty [d], Balint Alfoldy [e], Matic Ivančič [e], Martin Rigler [e], Asta Gregorič [e,g], Rok Podlipec [f,h], Svenja Lohmann [f], Gregor Hlawacek [f], Rene Heller [f], Ersin Tutsak [a], Griša Močnik [g,h,i]

[a] Environmental Science Center, Qatar University, P.O. Box 2713, Doha, Qatar
[b] Faculty of Mathematics and Physics, University of Ljubljana, Slovenia
[c] Climate and Atmosphere Research Center, The Cyprus Institute, Nicosia, 2121, Cyprus
[d] Qatar Environment and Energy Institute, Hamad Bin Khalifa University, Qatar
[e] Aerosol d.o.o., Sl-1000, Ljubljana, Slovenia
[f] Helmholtz-Zentrum Dresden-Rossendorf E.V., Institute of Ion Beam Physics and Materials Research, 01328, Dresden, Germany
[g] Center for Atmospheric Research, University of Nova Gorica, Sl-5000, Nova Gorica, Slovenia
[h] Jozef Stefan Institute, Sl-1000, Ljubljana, Slovenia
[i] Haze Instruments, Sl-1000, Ljubljana, Slovenia

HIGHLIGHTS

The text discusses a study focused on discriminating between aerosol mineral dust and BC absorption coefficients in various aerosol size fractions. The key highlights from the text are as follows:

- Collocated sites measurements: Measurements were conducted simultaneously at both an urban and a regional background site in Qatar using identical systems. Collocated Aethalometers were used, one with a virtual impactor and the other with a PM1 cyclone, to collect supermicron-enhanced and submicron aerosol fractions, respectively.
- Classification based on Optical Properties: The combination of aerosol absorption and scattering coefficient measurements allowed for the classification of particles based on the wavelength dependence of their optical properties, revealing the presence of BC internal/external mixing with various aerosols.
- Mineral Dust Contribution: HIM images provided information about the contribution of mineral dust in the submicron aerosol fraction. Absorption coefficients were determined during both dust storms and non-dust periods to calculate AAE for dust and BC.
- Source apportionment: Back-trajectories, wind regression, and PSCF were used to identify major regional sources of desert dust associated with northwesterly winds and major local BC sources associated with southerly west winds, with some offshore emissions transported by northeasterly and easterly winds.

ABSTRACT

Discriminating the absorption coefficients of aerosol mineral dust and black carbon (BC) in different aerosol size fractions is a challenge because of BC's large mass absorption cross-section compared to dust. Ambient aerosol wavelength dependent absorption coefficients (b_{abs}) in supermicron and submicron size fractions were determined with a high time resolution. The measurements were performed simultaneously using identical systems at an urban and a regional background site in Qatar. At each site, measurements were taken by co-located Aethalometers, one with a virtual impactor (VI) and the other with a PM1 cyclone to respectively collect super-micron-enhanced and submicron fractions. The combined measurement of aerosol absorption and scattering coefficients enabled the particles to be classified based on their optical properties' wavelength dependence. The classification reveals the presence of BC internally/externally mixed with different aerosols. Helium ion microscopy images provided information concerning the extent of mineral dust in the submicron fraction. The determination of absorption coefficients during dust storms and non-dust periods was used to establish the absorption Ångström exponent for dust and BC. Non-parametric wind regression, potential source contribution function and back-trajectory analysis reveal major regional sources of desert dust associated with north-westerly winds and a minor local dust contribution. In contrast, major BC sources found locally were associated with south-westerly winds with a smaller contribution made by offshore emissions transported by north-easterly and easterly winds. The use of a pair of Aethalometers with VI and PM1 inlets separates contributions of BC and dust to the aerosol absorption coefficient.

* Corresponding author. Environmental Science Center, Qatar University, P.O. Box 2713, Doha, Qatar.
E-mail address: mmkotb@qu.edu.qa (M.M.K. Mahfouz).

https://doi.org/10.1016/j.atmosenv.2024.120427
Received 16 November 2023; Received in revised form 24 February 2024; Accepted 26 February 2024
Available online 27 February 2024

1. Introduction

Black carbon (BC) is a primary atmospheric aerosol and a unique tracer of anthropogenic sources. Since it is formed during the incomplete combustion of carbonaceous fuels and is not chemically transformed in the atmosphere, it is typically found in the fine particle fraction (Bond et al., 2013). Common sources of BC are the industry, vehicular internal combustion engines, domestic heating and biomass burning. BC can cause direct environmental damage and is associated with adverse health effects (Bachmann, 2009; IARC P. 161, 2013). BC strongly absorbs light in the visible part of the spectrum, heats the atmosphere through absorption of solar radiation (IPCC and on, 2023). Unlike greenhouse gases, BC has a short lifetime in the atmosphere, with a reduction of emissions leading to a lowering of its atmospheric forcing within a few weeks (Bond et al., 2013).

In addition to carbonaceous aerosols, natural mineral dust efficiently scatters and absorbs solar radiation in the UV-blue part of the spectrum. This is especially important during desert storms when dust significantly adds to regional/global particulate concentrations (Liu et al., 2022; Yigiterhan et al., 2018). Around 11% of the global mineral dust mass load originates from the Arabian Peninsula (Tanaka and Chiba, 2006). Desert dust is mostly present in the super-micron fraction (Clarke et al., 2004) with a wide size range of 0.1 μm–100 μm and a typical mass-median diameter of 3.5 μm (Reid et al., 2003; Zhou et al., 2023). Through the processes of scattering and absorption, BC and desert dust interact with both incoming shortwave radiation and outgoing terrestrial longwave radiation (Sokolik and Toon, 1999).

Determining the wavelength-dependent aerosol absorption coefficient can be an effective tool for separating different light-absorbing aerosols, such as BC and dust. Among different BC measurement techniques, the Aethalometer (AE) has been widely used for decades (Hansen et al., 1982). The measuring of weakly light-absorbing dust can be more challenging given that BC features a much larger mass absorption cross-section than other aerosols (Bond et al., 2013) in the broad UV-IR spectrum, making the measurement of dust absorption difficult when BC is present (Drinovec et al., 2020). The highest mineral dust absorption, largely attributed to iron oxides, occurs at UV-VIS wavelengths (Alfaro et al., 2004; Di Biagio et al., 2017, 2019; Nakayama et al., 2021), with most measurements performed at shorter wavelengths (Izhar et al., 2020; H. Moosmüller et al., 2009; Zhao et al., 2019). Previous studies attempted to distinguish desert dust from BC using optical absorption of the transported African desert dust based on the difference between the absorption Angstrom exponent (AAE) of iron oxide (1.9 ± 0.2) and BC (1.0) with a two-component model (Fialho et al., 2005, 2014). The complete isolation of BC mass concentrations from other particulate matter light absorbers without interference is also challenging (Baumgardner et al., 2012; Mbengue et al., 2021). Measuring real-time aerosol absorption for different particle fractions requires a real-time particle--size separator device. Selective inlets like PM1 or PM2.5 cyclones allow separation of the aerosol fraction by particle size. Depending on the cyclone's design, particles smaller than a certain size can be effectively separated. Absorption of the submicron fraction, where BC absorption dominates, is much higher than that of the super-micron fraction, where dust dominates. This means that concentrating on the supermicron fraction will significantly increase the contribution of weakly absorbing desert dust relative to the strong absorption of fine BC in a mixed sample. The virtual impactor (VI) is a size selective inlet designed to concentrate particles in the super-micron fraction and provides a unique method for increasing the relative dust aerosol absorption when BC is present (Drinovec et al., 2020).

In the Eastern Arabian Peninsula (EAP) atmosphere, BC and desert dust mix in the ambient air. The composition of this mixture varies spatially (by proximity to urban sources or industry and desert), temporally (by time of the day and the season due to different meteorological conditions and events like dust storms) (Alfoldy et al., 2021). This study is the first to provide the high time-resolution absorption quantification of desert dust and BC dominated aerosols in the EAP atmosphere. The benefit of collocating both submicron and super-micron fraction sampling systems is that we can determine the respective desert dust and BC contributions to light absorption. Further, we investigate the optical properties of dust and BC components and separate their particular spectral dependency. The study provides unique insights into the classification of aerosols along with the feasibility of combining measurements of scattering and absorption spectral properties at urban and regional background sites in the EAP atmosphere. The presented study also estimates the transport routes of desert dust across the EAP and identifies local BC hotspots in the region.

2. Material and methods

2.1. Measurement locations

We conducted intensive real-time measurements of the optical properties of the ambient aerosol between 26 April and May 31, 2022 at two observatory sites in the EAP (Fig. 1). These sites were selected to represent urban and regional background environments. The urban background ("UB") site is characterized by limited contributions of local road traffic, ports and industry located within or near the campus of Qatar University with coordinates of 25°22′N 51°29′E. The second observatory site, chosen to represent regional background ("RB") is located at 25°41′N 51°34′E in Ras Matbakh, about 45 km north of the UB site. The RB site was selected due to its remoteness from local emission sources. Nevertheless, the two sites are located on the same path of air masses traveling from the surrounding desert that carry with them a mix of natural and anthropogenic aerosols. In particular, westerlies and southerlies may bring dust particles from the desert in Saudi Arabia and United Arab Emirates (Al-Dousari and Al-Awadhi, 2012; El-Baz and Makharita, 2016). Air mass transport from the north and the east may bring desert dust from Iraq and Kuwait as well as BC particles from combustion emissions from oil-transporting marine vessels (Comer et al., 2017), ports, onshore industry, and offshore installations such as oil platforms with flaring during oil and gas extraction (Nara et al., 2014; Villasenor et al., 2003).

To conduct the measurements, we employed four Aethalometers (Aerosol Magee Scientific, Model AE33). One sampling system at each site consisted of two Aethalometers running simultaneously, yet with different inlets. The first AE33 featured a PM1 cyclone (SCC 1.197, BGI Inc., USA) to collect the submicron aerosol fraction, while the other AE33 was equipped with a virtual impactor (VI) (Aerosol Magee Scientific) designed to enhance (concentrate) the aerosol super-micron fraction, as described by Drinovec et al. (2020) – the minor flow to the AE33 was 2 LPM while the total flow through the VI was 90 LPM. The light scattering of aerosol particles was measured at the UB site with a nephelometer (Aurora 4000, Ecotech) using a PM10 inlet. Additional equipment included an optical particle sizer (OPS 3330, TSI, USA) and a weather station with an anemometer to measure the direction and speed of wind (Davis Vantage Pro). The two aims of using OPS were to: 1) determine the site-specific VI enhancement factor; and 2) obtain measurements of aerosol optical diameter, assuming that optical diameter is equal to volume-equivalent diameter (Peters et al., 2006). The sections below describe the instrumentation used, their operation, and the data processing.

2.2. Instruments

2.2.1. Aerosol absorption

The Aethalometer (AE33) draws ambient air through a filter tape into which particles are continuously deposited and determines the light attenuation coefficient (b_{ATN}) by measuring the difference in light attenuation between the clean part of the filter and the sample spot during a given time period (Hansen et al., 1982, 1984). Attenuation due to the sample is the natural logarithm of the ratio between the light

intensities measured on the sample and reference detectors. The attenuation is thus caused by the deposited light-absorbing particles on the filter. The measurement is taken with 1-min time resolution. The 'true' absorption of the particles on the filter b_{abs} is lower than the measured b_{ATN} due to the scattering of light in the filter matrix, which lengthens the optical path in the filter and enhances the absorption compared to that of the same sample that would have been airborne.

This effect is parametrized by the multiple-scattering parameter specific for the filter and assumed for the M8060 filter as C = 1.39 (Aerosol Magee Scientific, 2018). Moreover, the gradual accumulation of absorbing particles on the loaded filter reduces the sensitivity, with this saturation being known as the filter-loading effect (Arnott et al., 2005; Coen et al., 2010; Drinovec et al., 2015; Weingartner et al., 2003). The AE33 provides dynamic filter-loading effect compensation based on a dual-spot measurement using two sample collection spots featuring different sampling flowrates (Drinovec et al., 2015).

The Absorption Ångström exponent (AAE) describes the spectral dependence of absorption by aerosols. It can be calculated from a selected wavelength pair, (λ_1) and (λ_2). AAE_i for aerosol size fraction i can be derived from the absorption coefficients according to the power law:

$$\frac{b_{abs,i}(\lambda_1)}{b_{abs,i}(\lambda_2)} = \left(\frac{\lambda_1}{\lambda_2}\right)^{-AAE_i} \quad (1)$$

Eventually, AE33 reports the mass concentrations of BC for seven wavelengths by dividing the absorption coefficient by the wavelength-dependent mass absorption cross-section (MAC):

$$BC(\lambda) = \frac{b_{abs}(\lambda)}{MAC(\lambda)} \quad (2)$$

where BC (λ) is the reported concentration of BC at λ, $b_{abs}(\lambda)$ is the absorption coefficient at λ and MAC (λ) is the BC mass absorption cross-section given to be 18.47, 14.54, 13.14, 11.58, 10.35, 7.77, and 7.19 m^2/g for the wavelengths 370, 470, 520, 590, 660, 880 and 950 nm, respectively (Aerosol Magee Scientific, 2018). Since organics and other light-absorbing aerosols have limited absorption at the IR wavelength, the reported concentration at 880 nm is considered to define

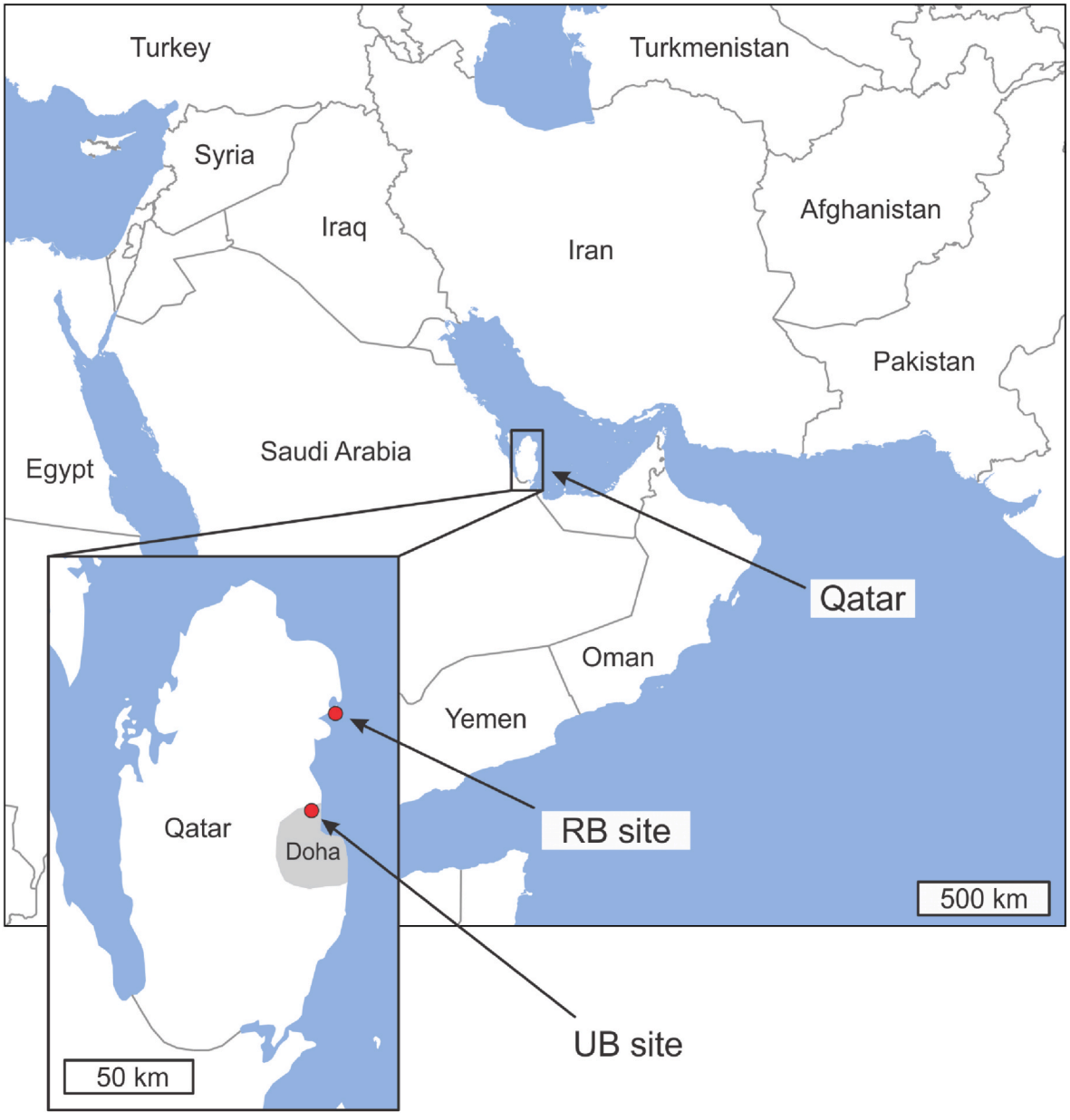

Fig. 1. Locations of the regional background (RB) and urban background (UB) sites.

'equivalent' BC (Drinovec et al., 2015; Zotter et al., 2017).

2.2.2. Aerosol scattering

Ambient PM10 scattering coefficient was measured at 1-min time resolution with an Aurora 4000 Nephelometer at three wavelengths; 450, 525 and 635 nm. We applied the correction for the angular truncation error accounting for the lack of illumination at extreme angles (near 0° and 180°) and for the slightly nonsinusoidal illumination function of the light source (Bond et al., 2009). Our method follows an angular correction based on the specific feature of the Aurora 4000 that integrates the angular scattering function at many different angular sectors, which were recently updated (Müller et al., 2011, 2012; Teri et al., 2021) as:

$$C_{polar} = \left(c + d \cdot \frac{b_{sct}^{Aurora,10} - b_{sct}^{Aurora,20}}{b_{sct}^{Aurora,10}} \right)^{-1} \quad (3)$$

where $b_{sct}^{Aurora,10}$ and $b_{sct}^{Aurora,20}$ are the scattering coefficients measured at angles 10° and 20°, and c and d are constants of values (1.043) and (−0.7651), respectively (Teri et al., 2021).

The scattering coefficients during the monitoring period were corrected for angular truncation error C_{polar}. The means of C_{polar} calculated for the Aurora 4000 wavelength domain of 450, 525 and 635 nm were determined to be 1.065 ± 0.03, 1.072 ± 0.03, 1.076 ± 0.04, respectively.

The truncation corrected scattering coefficients $b_{sct}(\lambda)$ in the nephelometer domain wavelength were used to extrapolate the scattering coefficients in the AE domain, i.e., 370, 470, 520, 590, 660, 880 and 950 nm, by calculating the scattering Ångström exponent (SAE) according to the equation:

$$\frac{b_{sct}(\lambda)}{b_{sct\ (635nm)}} = \left(\frac{\lambda}{635} \right)^{-SAE} \quad (4)$$

where $b_{sct}(635nm)$ is the total scattering coefficient at 635 nm, and SAE is calculated for the pair of 450 and 635 nm. The single scattering albedo (SSA) for each λ can be calculated from the scattering and absorption coefficient:

$$SSA = \frac{b_{sct}(\lambda)}{b_{abs}(\lambda) + b_{sct}(\lambda)} \quad (5)$$

2.2.3. Auxiliary measurements

Optical size distribution measurements were obtained via an optical particle sizer (OPS; TSI, model 3330). The OPS uses optics with 120° light collection for a size range of 0.3–10 μm in up to 16 channels (TSI Inc, 2022). The measuring time resolution of the OPS was set to an average of 1 min during the measurement period.

We performed continuous measurements in the monitoring period for ambient meteorological parameters, including wind speed and direction as well as relative humidity and temperature (Vantage2 Pro, Davis USA) at the UB site. All meteorological parameter measurements were averaged to 1 h and synchronized to the time-stamp provided by the optical measurements.

To unravel the distribution and physical properties of BC and desert dust collected on the filter fibers, a helium ion microscope was used (HIM, Orion NanoFab, Zeiss) (Hlawacek et al., 2014). HIM offers microscopic images with high spatial resolution, a large depth of field (DoF), while no specimen coating is needed to prevent any surface modification. The machine is equipped with a Gas Field Ion Source (GFIS) that provides very high source brightness, low divergence angle and a lateral resolution down to 0.5 nm, significantly outperforming Scanning Electron Microscopy (SEM) capability. Before imaging, filter fibers from the VI and PM1 inlets were cut in half and attached with carbon tape to the standard pins fit into a multi-pin specimen mount. Imaging in high vacuum mode was performed through the detection of ion-induced secondary electrons emitted from the surface layer of a few nm thickness. The chosen experimental parameters were 30 keV (helium ion energy), 400 fA (helium ion current) and $2x10^{-7}$ hPa (chamber vacuum). During the imaging, an integrated electron flood gun was used to neutralize the charge of the samples. Field-of-view (FoV) of the acquired images varied from 100*100 μm^2 to high magnification 4*4 μm^2 with a minimal pixel step size of 2 nm.

2.3. Data processing

2.3.1. Absorption coefficient in the submicron fraction

The determination of the absorption coefficient of the submicron fraction was calculated based on measurements with the AE33 attached to a PM1 cyclone (BGI, SCC 1.197). The PM1 cyclone has a cut-off point $D_{50\%} = 1$ μm aerodynamic equivalent particle diameter and was operating at a flow rate of 5 LPM. The absorption coefficients were calculated from the BC measurements by Eq. (2) with default MAC and C values. In this size fraction, the AE33 Aethalometer can provide effective dynamic compensation for a filter loading effect (Drinovec et al., 2015, 2017).

2.3.2. Two-component model (TCM)

To identify the potential contribution of dust in a submicron fraction, assuming the absence of a primary/secondary light-absorbing organic aerosol (brown carbon, BrC), we propose a two-component BC and dust absorption model. BrC and dust cannot be separated simply by looking at their optical properties (which are similar), so complementary techniques need to be used – we have employed helium ion microscopy (see below). The model follows the concepts of the widely accepted two-component model (Sandradewi et al., 2008; Zotter et al., 2017). In TCM, the aerosol absorption coefficient is the sum of all component absorption coefficients, with each featuring a component-specific power law (Moosmüller et al., 2009, 2011). In this case, the wavelength-dependent absorption coefficients for BC and dust at two wavelengths λ_1 and λ_2 are:

$$b_{abs,BC}^{PM1}(\lambda_2) = \frac{b_{abs}^{PM1}(\lambda_1) - b_{abs}^{PM1}(\lambda_2) * \left(\frac{\lambda_1}{\lambda_2}\right)^{-AAE_{dust}}}{\left(\frac{\lambda_1}{\lambda_2}\right)^{-AAE_{BC}} - \left(\frac{\lambda_1}{\lambda_2}\right)^{-AAE_{dust}}} \quad (6)$$

$$b_{abs,dust}^{PM1}(\lambda_2) = b_{abs}^{PM1}(\lambda_1) - b_{abs,BC}^{PM1}(\lambda_2) \quad (7)$$

where AAE_{dust} and $b_{abs,dust}(\lambda)$ are the absorption Ångström exponent and absorption coefficient for dust and AAE_{BC} and $b_{abs,BC}(\lambda_2)$ are the BC absorption Ångström exponent and absorption coefficient, respectively.

2.3.3. Absorption coefficient in the super-micron fraction

We used the virtual impactor (VI) at both sites to concentrate the super-micron size fraction. Detailed information on the VI operational principle and main characteristics is provided in the supplementary material and Drinovec et al. (2020). The reported BC from AE33 was used to calculate b_{ATN} throughout the entire wavelength domain (370–950 nm) by implementing Eq. (2). The initial b_{ATN} were compensated by the AE33 algorithm for the filter loading artifacts. Still, in this size fraction the automatic compensation to derive the corrected $b_{abs}(ATN)$ was not working properly, most likely due to the different depth distribution of the coarse particles in the filter matrix (Drinovec et al., 2015). To correct this behavior, we applied a post-processing linear regression to $b_{abs}(ATN)$ to obtain best-fit parameters and corrected b_{ATN} to obtain $b_{abs}(ATN)$ (Drinovec et al., 2015, 2020).

The VI concentrates the coarse particles (super-micron), whereas the smaller particles remain at the ambient concentration (Fig. S1). The dust absorption in the super-micron fraction was quantified by subtracting the BC contribution (not enhanced by the VI) from the absorption coefficient of the VI sample, normalizing it with the enhancement factor (EF) following the methodology in Drinovec et al. (2020):

$$b_{abs,dust}(\lambda) = \frac{b_{abs,VI}(\lambda) - b_{abs,BC}(\lambda)}{EF} \quad (8)$$

where $b_{abs,BC}(\lambda)$ is the absorption coefficient of the BC component in the submicron fraction that is unchanged by the VI inlet. Absorption by dust in the super-micron fraction is usually calculated at short wavelengths (370 nm) due to the stronger absorption of dust at short wavelengths and limited contribution of dust to the absorption coefficient at longer wavelengths. The VI enhancement factor EF for the super-micron particles depends on the VI minor/major flow ratio and the VI design, and is the ratio of the integral volume size distribution of the particles measured with the instrument after a VI inlet (V_{VI}) and one measurement of the ambient air without any size-selective inlets (V) obtained from the co-located OPS. Drinovec et al. (2020) reported an EF value of 11 ± 2 for a laboratory experiment using polystyrene latex (PSL) spheres with nominal aerodynamic sizes of 0.7–10 μm and a VI flow ratio F_{major}/F_{minor} of around 50. Detailed VI calculations may be found in the supplement.

We determined the required VI enhancement factor (EF) as the ratio of the integrals of the volume distributions with (V_{VI}) and without the virtual impactor (V) (Drinovec et al., 2020). Particle volume distributions obtained with the VI depend on its concentration enhancement factor (CE). CE is a particle-size-dependent factor calculated as the ratio of particle number concentrations measured with and without VI. The results of volume distributions of V and V_{VI} in addition to their ratio (CE) are presented in Fig. 2; more details of CE and EF calculations are available in the supplement. CE values in the submicron fraction (PM < 1.0 μm) show a non-significant increment compared to the super-micron fraction (1.0<PM < 10.0 μm), which confirms the VI ability to concentrate the large particle size fraction while maintaining constant concentration of the small size fraction. Fig. 2 also shows a maximum of VI concentration efficiency (CE) at the particle size 3.75 μm at both sites, similarly to results obtained by Drinovec et al. (2020). Results for EF obtained as 22.6 (UB) and 14.5 (RB) are close to the published values of a mean of 21 at a similar urban background site (Tohidi et al., 2022) and 11 ± 2 at a similar regional background site (Drinovec et al., 2020).

The volume size distributions at UB feature larger articles than at RB, which we interpret to arise from resuspension of coarse material by traffic in the city. This results in a higher CE at these large sizes and a higher value of EF at UB.

2.3.4. Aerosol classification scheme

We deployed the classification of different aerosol types according to Cappa et al. (2016) and as applied in several publications (Kaskaoutis et al., 2021; Romano et al., 2019; Schmeisser et al., 2017; Valentini et al., 2020). Threshold values for SAE and AAE were applied to discriminate aerosols by size and composition. The threshold of SAE>1 indicates the small (submicron) fraction, while SAE<1 points to a large (super-micron) size fraction (Cappa et al., 2016). Compiling AAE/SAE values gives insights into different aerosol categories where AAE>2.0 and SAE>1.5 correspond to fresh smoke aerosols favoring light-absorbing primary organic aerosol ('brown carbon', BrC) and decreased AAE values can be attributed to aged BC or a long-range transported mix with other aerosols (Diapouli et al., 2014). The intermediate values of 1.5 < AAE <2.0 and the fine aerosols (SAE> 1.5) indicate a mixture of BrC/BC, while particles of a larger size (SAE<1) could point to mixtures with desert dust, characterizing the "dust-mix" type. The pure mineral dust (desert) yields AAE values ranging from 1.5 to 6.5 (Petzold et al., 2009; Yang et al., 2009) with a large particle size (SAE<0.5) (Romano et al., 2019). However, SAE<1 for large (super-micron) particles with low absorption spectral dependence (AAE<1) are typical sea salts (Hess et al., 1998), while smaller particles (SAE >1) are characterized by small (submicron) particles like secondary inorganic aerosols (Romano et al., 2019; Zhang et al., 2012). Furthermore, the graphical framework utilizing AAE in conjunction with SAE and color-coded according to the difference in Single Scattering Albedo (dSSA) has demonstrated effectiveness as a classification scheme for distinguishing various types of particles and particle mixtures (Costabile et al., 2013; Romano et al., 2019).

2.3.5. Non-parametric wind regression (NWR) and potential source contribution function (PSCF)

Many apportionment studies investigate the geographical origins of atmospheric pollutants based on wind data and backward trajectories. We used the Openair package in R (Carslaw and Ropkins, 2012) to identify the likely paths of the air mass transported to the monitoring sites. The Openair package was used for the non-parametric wind regression (NWR) method, which can identify and quantify the impact of possible source regions of pollutants as defined by wind direction sectors. For details of the principles underlying the NWR calculation and its analysis, we refer to Henry et al. (2009). We used the ZeFir toolkit (Petit et al., 2017a) to calculate and analyze air mass back trajectories derived

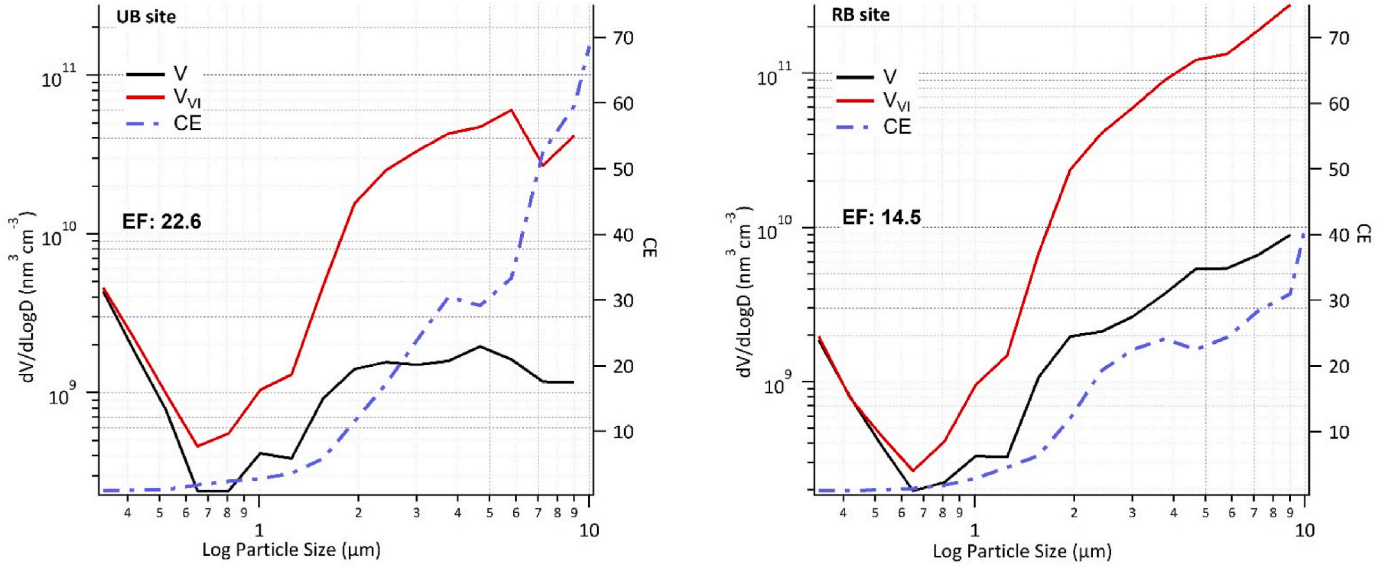

Fig. 2. Average volume size distribution by OPS without and with VI (V and V_{VI}, respectively) and concentration enhancement (CE) alongside particle size at both sites on a log/log scale.

via the HYSPLIT model (Draxler, 2018). Wind field information was obtained from the Global Data Assimilation System (GDAS, NOAA, 2019) with a 1° spatial resolution. The ERA5 reanalysis dataset (Hersbach et al., 2020) was implemented to visualize and analyze the wind fields to understand the spatial movements of the air in the region and perform the back-trajectory analysis.

The PSCF method in the ZeFir toolkit examines air mass trajectories to investigate potential transport routes of pollution over large geographical areas. PSCF indicates potential source regions contributing high air pollutant concentrations based on the total number of trajectories over a given geographic region and the number of trajectories to high air pollutant concentrations at the receptor, assuming no loss through diffusion, chemical transformation or atmospheric scavenging (Cheng et al., 1993; Petit et al., 2017b). In our application, we constrained a threshold percentile of 60% of the absorption coefficients, a grid cell resolution of 0.03° in addition to GDAS NOAA wind fields to produce a PCSF model at the UB site. More information on PSCF may be found in the supplementary information.

2.3.6. ERA5 wind streamlines

Meteorological parameters like wind speed and direction are essential tools for understanding the dynamics of air pollutant movements. In this context, we can draw and visually analyze wind streamlines. A streamline is a line with its tangent at any point in a fluid (in this case, air) parallel to the instantaneous velocity of the fluid at that point (American Meteorological Society, 2022). It is a tool for visualizing and analyzing the spatial movements of the air at a given moment in time. Streamlines were calculated from the 10 m height wind parameter in the widely used ERA5 reanalysis dataset (Hersbach et al., 2020).

3. Results of the study

3.1. Overview of the measurements

The focus of our study was on dust-dominated and BC-dominated particles among all aerosol types. Our assessment considered special dust events where dust is abundant in the atmosphere, i.e., dust storms. Dust storms in the EAP usually occur during hot periods (April to August). During the monitoring period, the EAP was influenced by two major dust storms that caused significant variations in absorption and scattering measurements as recorded on 17–18 and 24–25 May 2022. Air masses travelled during these two events from the north to the monitoring sites (NASA, 2022).

Fig. 3 shows a sequence of streamline images at the onset of the two dust storm events. The top panel in each subfigure shows the super-micron and submicron fraction absorption coefficients at 370 nm for 10 days (Fig. 3a1 and 3b1), while the lower panels show a sequence of streamline images at the onset of the dust storms (Fig. 3a2–3a4 and 3b2–3b4). The light absorption of the supermicron size fraction increased significantly during both dust events at both measurement locations while submicron light absorption stayed almost unchanged (Fig. 3a1 and 3b1). This is consistent with numerous studies conducted in the Mediterranean where the long-transported dust is always in a super-micron fraction (Coen et al., 2004; Ealo et al., 2016; Pandolfi et al., 2011). The timing of the significant increase in the super-micron fraction corresponds to the increase in wind speed over the Qatari peninsula (Fig. 3a3 and 3b3). At the time the dust storm was arriving, the wind speed exceeded 9 m/s. In both events, strong winds blew from the NW direction (Fig. 3a3–3a4 and 3b3–3b4). The received desert dust could be regionally transported or locally suspended given that both sites are located on the eastern shore and the strong wind could lift the dust particles of the ground as air moves across the peninsula before reaching the measurement sites. For both events, a strong NW wind first appeared over Syria, Iraq, Jordan and the northern part of Saudi Arabia prior to moving to the Arabian Gulf and Qatar (Fig. 3a2 and 3b2). This means that some of the dust particles measured in Qatar may have originated from far away. In this context, as described below, we processed and analyzed the data separately for three periods: dust storm (DS), non-dust storm (NonDS) and the whole monitoring period (All days).

The two major dust storms led to a large increase in the scattering and absorption coefficients (Fig. 4). During these storms, the scattering coefficient increased by more than 10 times relative to the average baseline of the background (Fig. 4a) while the increase was even bigger for the absorption coefficient (Fig. 4b). Both the scattering and the absorption coefficient were strongly wavelength-dependent. Large change in the SAE (450/635 nm) was observed (Table 1), with the SAE value negative for DS periods and positive otherwise. SAE <1.0 in the three periods indicates the predominance of large particles where the negative value during DS is consistent with storm conditions (Valenzuela et al., 2015).

The SSA (Table 1) also changes considerably during the three periods, with values 0.83–0.93 (DS), 0.69–0.79 (NonDS), 0.70–0.79 (All days). The significant variations of the scattering and absorption during DS and NonDS highlight the large difference in particle sizes and composition in these periods. During DS periods, the SSA wavelength dependence as parametrized by its Ångström exponent SSAAE (450/635 nm) features more negative values (-2.06), as expected for desert dust events (Colaud Coen et al., 2004), than during the non-DS periods (-0.98). The negative average of SSAAE throughout the measurement period indicates that suspended dust is a constant in the atmosphere. In line with the SSAAE (450/635) findings, the positive sign of the parameter dSSA (660–370) during all three monitoring periods, as indicated in Table 2, primarily points to the prevalence of aerosols with large particle sizes (super-micron) (Dubovik et al., 2002).

The AAE was calculated for the submicron and super-micron size fractions at three pairs of wavelengths: 1) short wavelength domain (370/590 nm); 2) long wavelength domain (660/950 nm); and 3) mid-range domain (470/880 nm) in addition to 370/950 nm (Table 2). In the short wavelength pair (370/590 nm), the highest absorption spectral dependence of the super-micron fraction (AAE $= 3.46 \pm 0.15$) was found during DS, indicating the strong influence of dust compared to the NonDS periods at both locations, comparing well with the published values (Drinovec et al., 2020). The probable influence of dust on AAE during DS decreases at the longer wavelength pair (470/880 nm) to the value AAE $= 2.10 \pm 0.12$ due to the decreased absorption induced by dust at the longer wavelengths. The minimum AAE (i.e., 0.59 ± 0.09) was found for the 660/950 nm pair since dust in this region exhibits very low absorption. The super-micron AAE (370/950 nm) during the DS periods shows a mean of 2.14 ± 0.08 (UB) and 2.10 ± 0.08 (RB).

The AAE in the submicron fraction features much smaller variation while their differences between the periods at the two sites may imply a different mixture of sources. The long wavelength absorption is dominated by BC from fossil fuel combustion (Kirchstetter et al., 2004; Massabò et al., 2015; Yang et al., 2009; Zotter et al., 2017). The AAE trend in the submicron fraction, similar to AAE super-micron fraction at the short wavelength domain, may also show the contribution of dust in this small size fraction. The existence of dust particles in the submicron fraction size is a tail of the dust size distribution, however it is much more prominent in the super-micron fraction.

The assessment of BC and other aerosol contributors (i.e., dust) in the submicron fraction samples was first conducted by analyzing images taken by high-resolution Helium Ion Microscopy (HIM) (Scipioni et al., 2008). Fig. 5 displays the most representative HIM images. BC denoted with yellow arrows features typical fractal chain-like structures (Fig. 5 A) as well as micron-sized aggregates (Fig. 5 B), showing different ageing and sources of the pollution. Typical dust particles are observed as elongated shapes with rough surfaces and average sizes close to 1 μm^2 (blue arrows in Fig. 5), whereas the much smaller particles in the form of rounder shapes and less rough surfaces probably correspond to organic aerosols or inorganic sea salt particles (red arrows in Fig. 5). To better visualize and characterize the particles' shapes and morphologies,

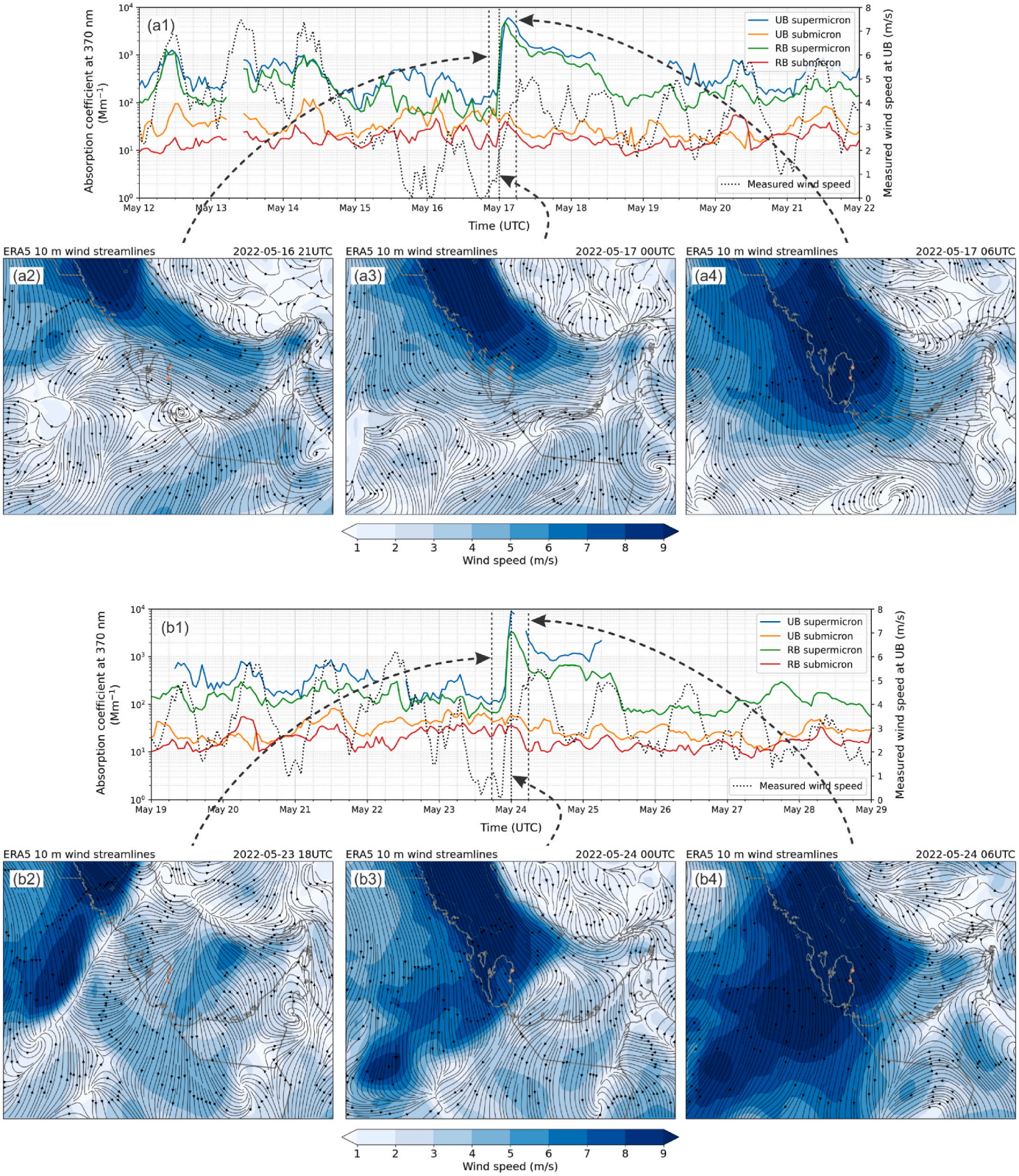

Fig. 3. Subplots (a1) and (b1) show the time series of super-micron and submicron absorption coefficients at 370 nm at both sites (labelled UB and RB) in a 10-day period. Subplots (a2)–(a4) and (b2)–(b4) contain ERA5 10 m wind streamlines at the onset of two dust storms on 17 May and 24 May, respectively. The time corresponding to each streamline image is marked with a dotted vertical line on the graph with the time series of the measured optical absorption.

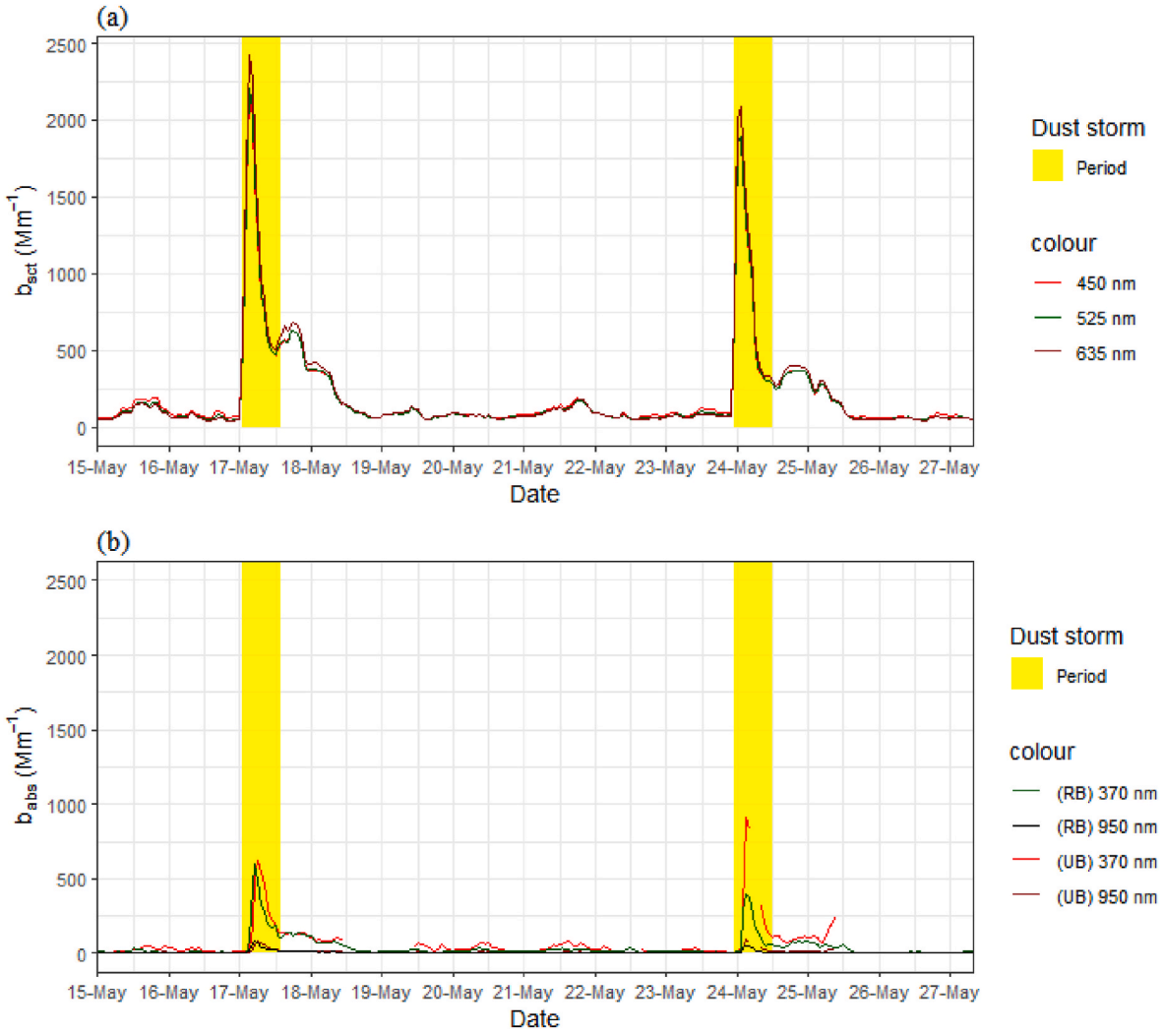

Fig. 4. Daily variation of: (a) scattering coefficients; and (b) absorption coefficients of the super-micron size fraction at the UB and RB sites. The approximate start and end time of dust storms are marked with yellow. Dust storm time selection is based on observation of exaggerated scattering and absorption coefficients (Mm^{-1}) (e.g., >10 x of the average background).

Table 1
Mean SSA (λ) and SAE (450/635 nm) values with standard deviation in brackets for the super-micron size fraction at the UB site, along with derived SSAAE (450/635) and dSSA (660-370 nm) values during the three monitoring periods.

Parameter	DS N = 79	NonDS N = 789	All days N = 868
SSA (470 nm)	0.83 (0.05)	0.69 (0.10)	0.70 (0.11)
SSA (520 nm)	0.88 (0.03)	0.73 (0.10)	0.74 (0.11)
SSA (660 nm)	0.93 (0.02)	0.77 (0.11)	0.79 (0.11)
SAE (450/635)	−0.22 (0.10)	0.38 (0.39)	0.32 (0.41)
SSAAE (450/635)	−2.06 (0.23)	−0.98 (0.60)	−1.06 (0.65)
dSSA (660–370)	0.24 (0.07)	0.14 (0.08)	0.15 (0.08)

highly magnified imaging was followed with the FoV of just a few square microns (Fig. 5 C, D). Submicron mineral dust particles were found to be highly heterogeneous, locally showing rod-shaped aggregated structures with rod-like extensions at the boundaries (Fig. 5 B, C; white-blue arrow). Smaller, presumably sea salt, particles ranging from 0.1 μm^2 up to 0.5 μm^2 in size were also found in the mixture with BC aggregate (Fig. 5 D; red arrow). HIM imaging was also performed on the VI inlet samples with a super-micron fraction of collected particles (Fig. 5 E, F). The images that reveal the extensive dust population throughout the filters also show the presence of large BC aggregates (yellow arrows) with the magnified inset presented in Fig. 5 F. Finally, using HIM, we were unable to find large circular-like Tar particles, confirming our assumption of negligible BrC in the aerosol samples collected.

3.2. Aerosol classification scheme

We applied the aerosol classification scheme suggested by Cappa et al. (2016) for overall days for the hourly averages of $AAE_{(370/950)}$ versus $SAE_{(450/635)}$. Based on the SAE/AAE ratio, aerosols in the EAP were placed into 8 classes: Dust_dom (pure dust), MBCD (mixed BC/dust), LPBC (large particles/BC mix), LPLA (large particle/low absorption), SPLA (small particles/low absorbance), BC_dom (BC-dominated aerosols), MBCBrC (mixed BC/BrC) and StrBrC (pure strong BrC). Results of the classification are presented in Fig. 6. The illustrated classification matrixes, color-coded by wavelength dependence dSSA = $SSA_{370} - SSA_{660}$, are shown in Fig. 6a and b for the urban and background sites, respectively. Positive dSSA values are mostly linked with aerosols or mixtures of a large (super-micron) size (SAE <1), while the negative ones accompanying the fine (submicron) size aerosols (SAE >1) indicate the greater presence of BC (Dubovik et al., 2002).

Fig. 7 shows the frequencies of identified classes for each site. We can observe comparable results between the two sites: class LPBC, with a spectral signature of 1.0 < AAE <1.5 and SAE <1.0, dominates at both

Table 2
Different *AAE* (standard deviation) for the two aerosol size fractions at the UB and RB sites.

Wavelength range (nm)	Size fraction	Urban site			Regional site		
		DS N = 79	NonDS N = 789	All days N = 868	DS N = 79	NonDS N = 789	All days N = 868
370/590	**Super-micron**	3.46 (0.15)	2.69 (0.45)	2.75 (0.49)	3.39 (0.16)	2.77 (0.40)	2.83 (0.42)
470/880		2.10 (0.12)	1.69 (0.27)	1.72 (0.29)	2.06 (0.08)	1.75 (0.22)	1.78 (0.23)
660/950		0.59 (0.09)	0.62 (0.08)	0.61 (0.08)	0.57 (0.05)	0.60 (0.08)	0.60 (0.08)
370/950		**2.14 (0.08)**	**1.72 (0.25)**	**1.76 (0.27)**	**2.10 (0.08)**	**1.77 (0.21)**	**1.80 (0.22)**
370/590	**Submicron**	1.50 (0.34)	1.27 (0.39)	1.29 (0.39)	1.25 (0.24)	1.08 (0.31)	1.10 (0.30)
470/880		1.25 (0.14)	1.17 (0.13)	1.17 (0.14)	1.23 (0.10)	1.16 (0.17)	1.17 (0.16)
660/950		0.97 (0.05)	0.94 (0.06)	0.94 (0.06)	1.01 (0.06)	0.98 (0.18)	0.98 (0.18)
370/950		**1.27 (0.19)**	**1.14 (0.20)**	**1.15 (0.20)**	**1.16 (0.13)**	**1.06 (0.19)**	**1.07 (0.19)**

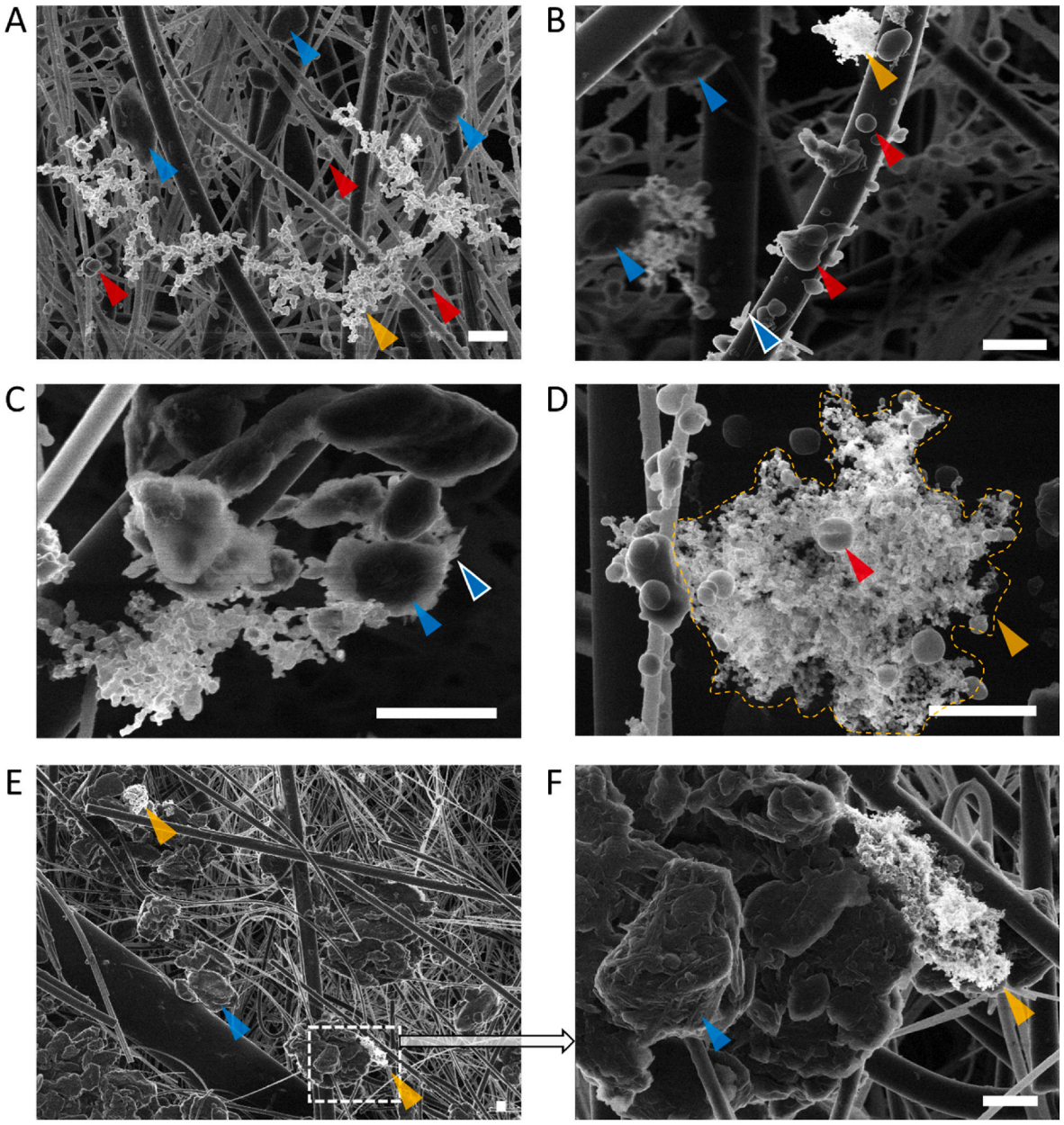

Fig. 5. Representative high-resolution HIM images of predominantly submicron-sized particles collected from PM1 inlet (A–D) and predominantly super-micron-sized particles collected from VI inlet (E–F). Images show the presence and detailed morphologies of BC (brightest particles) with their aggregated form (yellow-dashed region and arrows), mineral dust (blue arrows) and probable organics and sea salt particles (red arrows). The scale bar is 1 μm.

locations with shares over 50%. This class mostly contains aged BC particles as internal mixtures due to the photochemical oxidation of ambient VOCs during the daytime. It is notable that coating BC, known as the "lensing effect" (Hans Moosmüller et al., 2012; Kalbermatter et al., 2022; Shamjad et al., 2018), can increase its spectral dependence AAE by up to 1.5 depending on different core-to-shell thickness ratios.

The LPBC is followed by the MBCD class, with an approximate share of 30% for both sites. This suggests that dust is frequently present in the air over the EAP, also outside of dust storms. Our measurements are consistent with findings that most of the dust and BC particles are mixed externally/internally with other pollutants (Bond and Bergstrom, 2006; Yus-Díez et al., 2022).

The Dust_dom class was completely related to the dust storm periods and shows a limited contribution of approximately 3%. The typical classification threshold for dust (SAE -1.0:0.25, AAE >2 and positive dSSA) is consistent with published literature concerning other locations (Costabile et al., 2013; Dubovik et al., 2002; Ealo et al., 2016; Kaskaoutis et al., 2021; Valentini et al., 2020).

Urban emissions at the UB site show a higher BC contribution in the BC-dominated aerosols class (BC_dom) (5%) compared to the RB site (3%). However, its proximity to the shoreline means that BC_dom at the regional site (RB site) perhaps also shows the influence of BC-rich

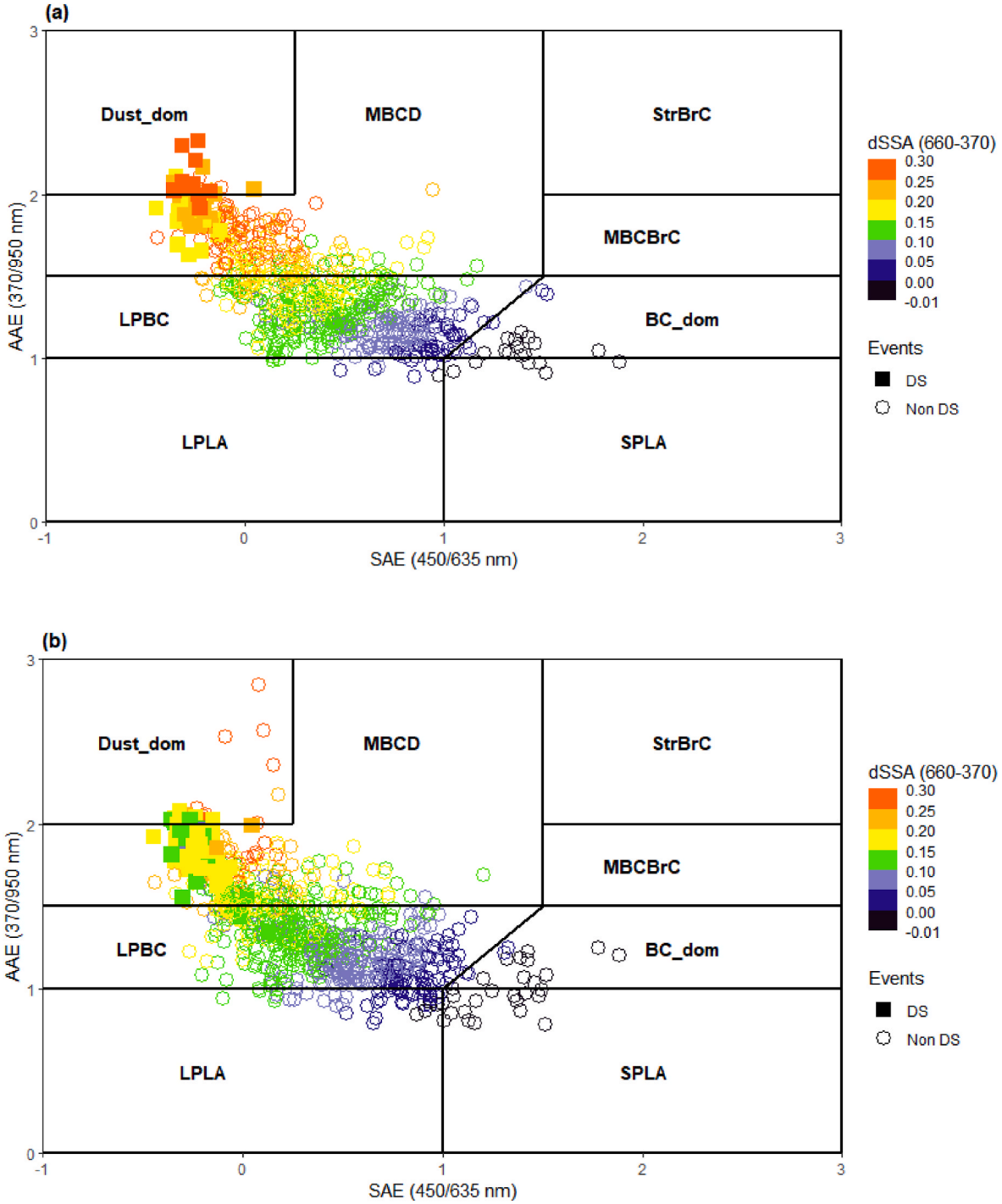

Fig. 6. Super-micron fraction optical classification scheme for $SAE_{450/635}$ and $AAE_{370-950}$ suggested by Cappa et al. (2016) coded by $dSSA_{660-370}$ at the (a) urban (UB) and (b) regional (RB) sites. Periods with dust storms are marked with filled squares, while other periods are indicated with circles.

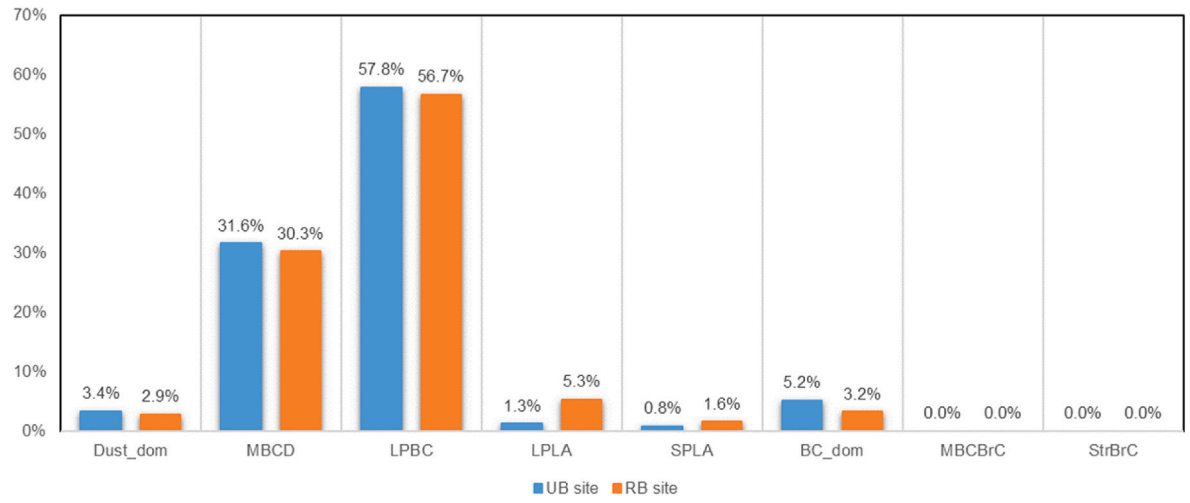

Fig. 7. Frequency of identified aerosol classes according to the optical scheme classification for both sites shown in Fig. 6.

marine emissions from shipping or flaring during upwind emissions at offshore platforms. It should be noted that the RB site is a coastal type, while the UB site is an inland located 4 km from the shoreline.

Although small particles/low absorbance (SPLA) have low spectral dependence (AAE<1), they scatter solar radiation significantly (SAE >1). SPLA appeared at 1% (UB) and 2% (RB) during the measurement periods. The particles in this class do not include BC but water-soluble inorganics particles like sulphates, nitrates or ammonium (Romano et al., 2019; Zhang et al., 2012). It is worth noting that BC particles and PM gas precursors (such as SO2 and NOx) are co-emitted by transportation sources into the atmosphere in urban areas. This may facilitate rapid heterogeneous interactions between BC particles and these gases. The photo-oxidation process of urban SO2 and NOx gases are major sources of these inorganic particles at the urban site. The greater abundance of small non-absorbing aerosol at the RB site could be due to sulphur emissions along marine routes and offshore platform flaring, and marine sources of organic aerosols.

The physical and optical features of large particle/low absorption (LPLA) include large-size aerosols (SAE<1), wavelength-independent SSA (dSSA = 0) and weak spectral dependence of the absorption (AAE<1). The relatively higher time percentage of LPLA at the RB site (5%) than the UB site (1%) corresponds to higher non-absorbing particles like sea salts. The higher abundance of non-absorbing particles at the RB site may indicate the influence of marine salts and minimal combustion activities (Hess et al., 1998). Marine salts, regarded as the largest aerosols emitted into the atmosphere indirectly through the evaporation of sea surface spray, are predominantly comprised of chlorides and sulphates. On the other hand, the existence of LPLA at both sites could be the result of the reaction of sea-salt particles and anthropogenic gases, alongside other types of aerosol particles, which change their compositions as Na-sulphate or Na-nitrate. For example, $NaNO_3$ may be formed as a result of anthropogenic nitric acid with sea salt, which results in extra coarse particles (Lewandowska and Falkowska, 2013).

The shares of the MBCBrC and StrBrC classes were negligible, suggesting the absence of BrC in the EAP region, as was also expected due to the minor use of biomass in the region.

3.2.1. Absorption coefficients for dust and BC

The absorption of dust is determined as the absorption of super-micron particles, with the submicron particle absorption coefficient subtracted and normalized by the enhancement factor, as in the model in Eq. (8) (Drinovec et al., 2020; Tohidi et al., 2022). In the original model developed by Drinovec et al. (2020), the submicron particle absorption signal is expected to be dominated by BC. However, this is not the case in the EAP region, as may be seen in the HIM images (Fig. 5) and the computed AAE using different wavelength domains (Table 2). These results show that dust makes a non-negligible contribution to the absorption coefficient in the submicron fraction. Therefore, the TCM model (Eqs. (6) and (7)) was used to split the absorption coefficient of the fine fraction into BC and dust, assuming BrC absorption is negligible in the EAP region, as shown previously (Fig. 6). The TCM model has two free model parameters – AAE_{BC} and AAE_{dust}. We took $AAE_{dust} = 3.46$ from Table 2 (super-micron fraction, dominated by dust, values similar at both sites), determined during a DS event when the domination of dust was exceptional. AAE_{BC} was considered to be equal to 1 (Fialho et al., 2005).

In previous sections, we showed that dust is the major contributor to aerosol optical absorption during DS. In Fig. 8, we can see that dust also contributes importantly during Non-DS periods. Fig. 8 shows typical diurnal profiles of the absorption coefficient apportioned between BC and dust for non-DS periods. We may observe a strong morning BC peak at the UB site (Fig. 8a) of up to 50 Mm^{-1}. The morning peak of BC typically results from the morning rush hour coinciding with Planetary Boundary Layer (PBL) height which has just started increasing. Daily fluctuations in PBL heights have the potential to modify BC mass concentrations through dilution, offering an explanation for the absence of an afternoon BC peak in both sites (Yuval et al., 2020). The morning peak of BC at the RB site (Fig. 8b) is lower and not so dominant, which suggests the local sources at the site are not strong or many. Both sites are characterized by an afternoon peak of the absorption coefficient apportioned to dust. The source of dust on Non-DS periods could be local resuspension and wind-driven erosion of the local dust. On afternoons, higher wind speeds are typical due to costal winds, as may be confirmed with diurnal typical diurnal profiles of wind speeds, shown in Fig. S3 in the supplement. The values of the afternoon absorption coefficient peak at 370 nm apportioned to dust almost reaches the morning BC peak values at the UB site (Fig. 8a), while it exceeds the BC morning peak at the RB site (Fig. 8b).

The normalized (number of observations) frequency distributions of the computed $AAE_{370/950}$ for the submicron fraction of dust (orange) and BC (grey) at both sites and illustrated in (Fig. 9), show the clear separation of BC and dust during DS and slightly overlapping distributions during non-DS at both sites. For DS, the dust $AAE_{370/950}$ is identical at both sites and also identical to the values obtained for the super-micron fraction during DS (Table 2), allowing us to conclude that the same dust is present at the RB and UB sites. The BC $AAE_{370/950}$ at both sites is the same for DS and NonDS. However, the values vary at each individual site during DS compared to the NonDS periods. The observed variation can be elucidated by considering the substantial amount of desert dust

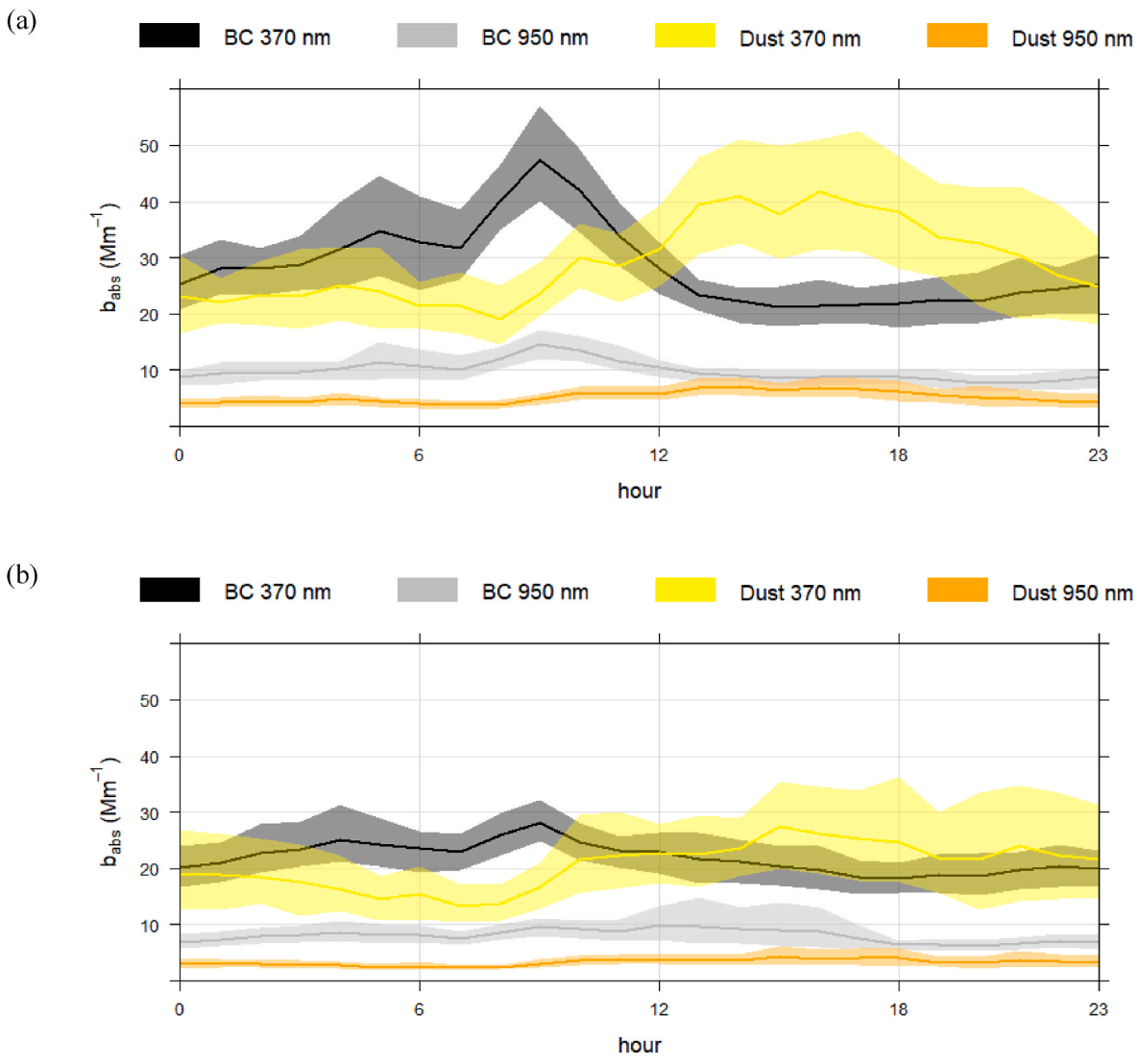

Fig. 8. Diurnal profiles of the absorption coefficient apportionment to BC and dust at (a) UB site and (b) RB site during NonDS periods.

present during DS periods. This abundance of desert dust may contribute to the depletion or masking of the absorption attributed to the concentration of particle/BC mix in the atmosphere.

At both sites, the dust $AAE_{370/950}$ features the clear contribution of different peaks, which we interpret as dust with BC particles attached to them (e.g., Fig. 5C). The BC on dust lowers the effective $AAE_{370/950}$ of such mixed particles. The mixing appears to be the same at both sites. Dust particles, laden with a significant amount of BC, exhibit similarities for Non-DS periods on both sides. However, variations become apparent during DS periods. During these periods, the presence of BC particles attached to dust leads to a slightly lower dust AAE in the UB site compared to the RB site.

3.3. Non-parametric wind regression

To determine the probable pathways of the air masses reaching the monitoring sites, we employed non-parametric wind regression (NWR), which is integrated within the Openair R package (Carslaw and Ropkins, 2012). NWR facilitated the identification of wind direction and speed associated with varying absorption coefficients linked to both BC and dust components. The NWR plots, as depicted in Fig. 10a and c, illustrate that heightened dust absorption at 370 nm is correlated with winds blowing from the northwest (2–8 m/s) at both locations (these strong winds are associated with dust storms that occurred on 17 May and 24 May), as well as the resuspension of dust due to topsoil erosion (Denier van der Gon et al., 2010). Notably, the region surrounding the Arabian Gulf is characterized by extensive superficial Aeolian sands distributed sporadically in the form of mobile, thin sand sheets and sand dunes (Yigiterhan et al., 2018). Consequently, the dust absorption coefficient (370 nm) at both sites is influenced by dust transported regionally through dust storms and locally generated by resuspension.

In the case of BC absorption at 950 nm, the NWR results indicate that dust may have a limited association, particularly at relatively high wind speeds (4–8 m/s) observed at the UB location. However, under lower wind speed conditions (<2 m/s), the NWR plot for BC absorption at the UB site (Fig. 10b) suggests the likely contribution of local sources from the southwest direction, which differs from the northwesterly dust sources. Additionally, at the regional site, there is evidence of urban influences, as a minor increase in BC absorption is observed with a southwest wind direction (Fig. 10d).

It is crucial to emphasize that the marginal rise in BC absorption coefficients at 950 nm, observed in conjunction with northeasterly (UB) and easterly (RB) wind directions (as illustrated in Fig. 10b and d), suggests a likely influence of BC transported from offshore platforms and oil tankers located upstream. To gain a more comprehensive understanding of regional and local sources of BC, we conducted air mass back

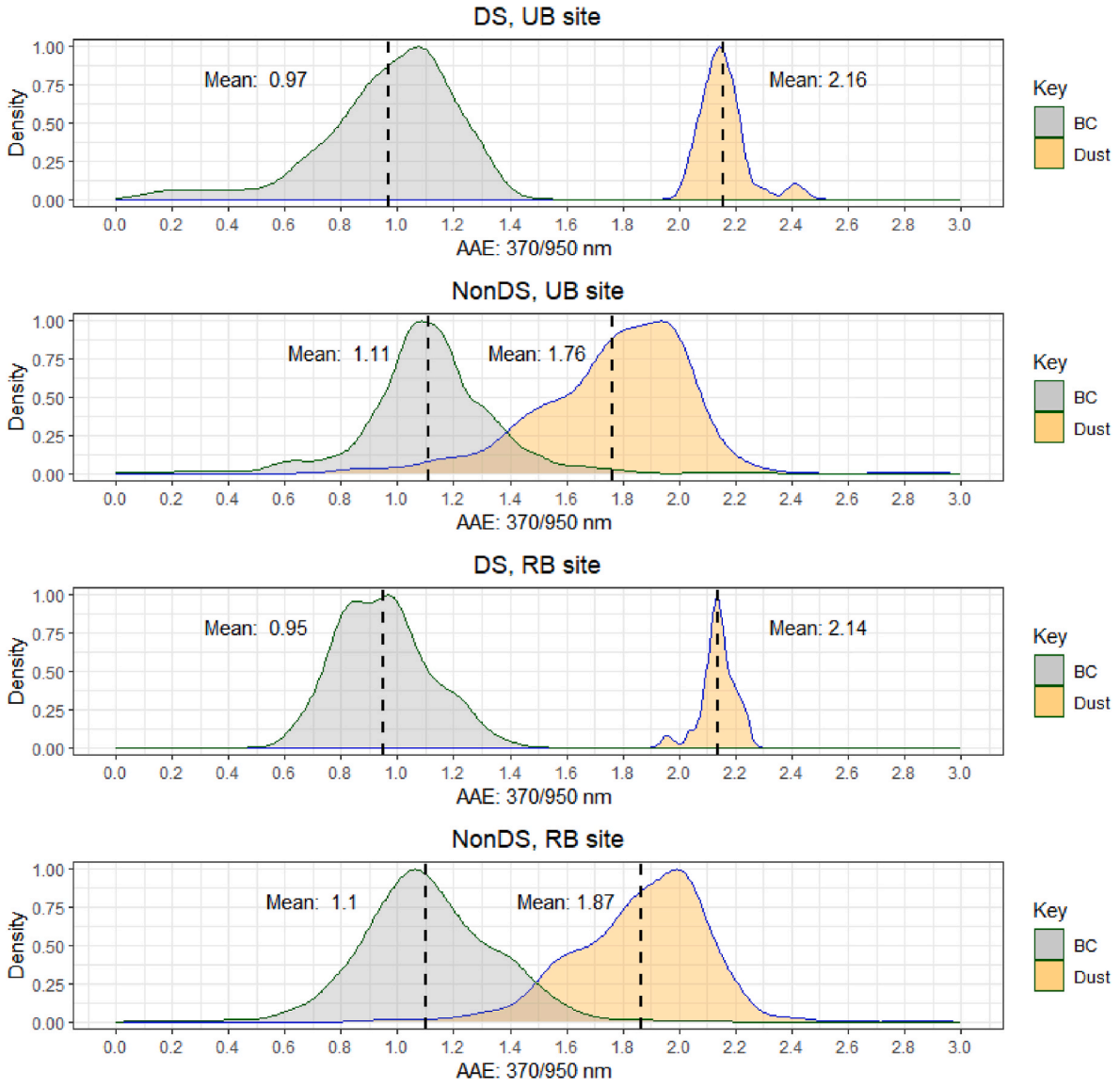

Fig. 9. Dust and BC-dominated $AAE_{370/950}$ during DS (upper panel) and NonDS (lower panel) periods; black dashed lines indicate the mean AAE of dust and BC distributions.

trajectory analysis using clustering techniques, as detailed in the supplementary material. In the subsequent section, we also present the results of PSCF analysis for a more thorough assessment.

3.4. Potential source contribution function

In order to identify the potential regional influences contributing to the observed absorption, we conducted a PSCF analysis using the ZeFir toolkit (Petit et al., 2017b) that utilizes 48-h back trajectories calculated via the HYSPLIT model (Draxler, 2018). Fig. 11 presents the PSCF results for the UB site for the BC absorption coefficients at 950 nm during the periods without dust storms (NonDS). PSCF findings reveal a significant probability/concentration density exceeding 0.5, suggesting potential local anthropogenic sources (e.g., city roads) primarily situated to the south of the UB site. Furthermore, there is a lower contribution of BC (with probability density ranging between 0.3 and 0.4) originating from long-range transport. This long-range BC is likely a result of anthropogenic activities in neighboring countries and is associated with a northwest direction. Additionally, the plot indicates a notable contribution with significant probability density from the eastern and northeastern directions, indicating potential emissions from dispersed offshore sources such as marine vessel routes.

4. Conclusion

This study achieved a high-time resolution separation of dust and BC absorption coefficients in two distinct aerosol fractions: super-micron and submicron. Utilizing co-located measurements of aerosol absorption and scattering, a classification scheme was implemented to discern various aerosol types. The aerosol classification scheme, coupled with qualitative HIM observations and frequency distribution plots of the AAE, strongly supports the notion that BC and dust are frequently mixed, which occurred approximately 90% of the time during the monitoring period. This mixing involves varying levels of BC attachment to dust particles. The scheme indicates that the coexistence of LPBC occurs approximately 58% of the time at the UB site and 57% at the RB site, while MBCD takes place in 32% of cases at the UB site and 30% at the RB site. Throughout the measurement period, a relatively small contribution of pure dust-dominated aerosols (3% at both sites) and BC-dominated particles (5% at the UB site and 3% at the RB site) was observed.

During NonDS periods, the BC absorption coefficient displayed

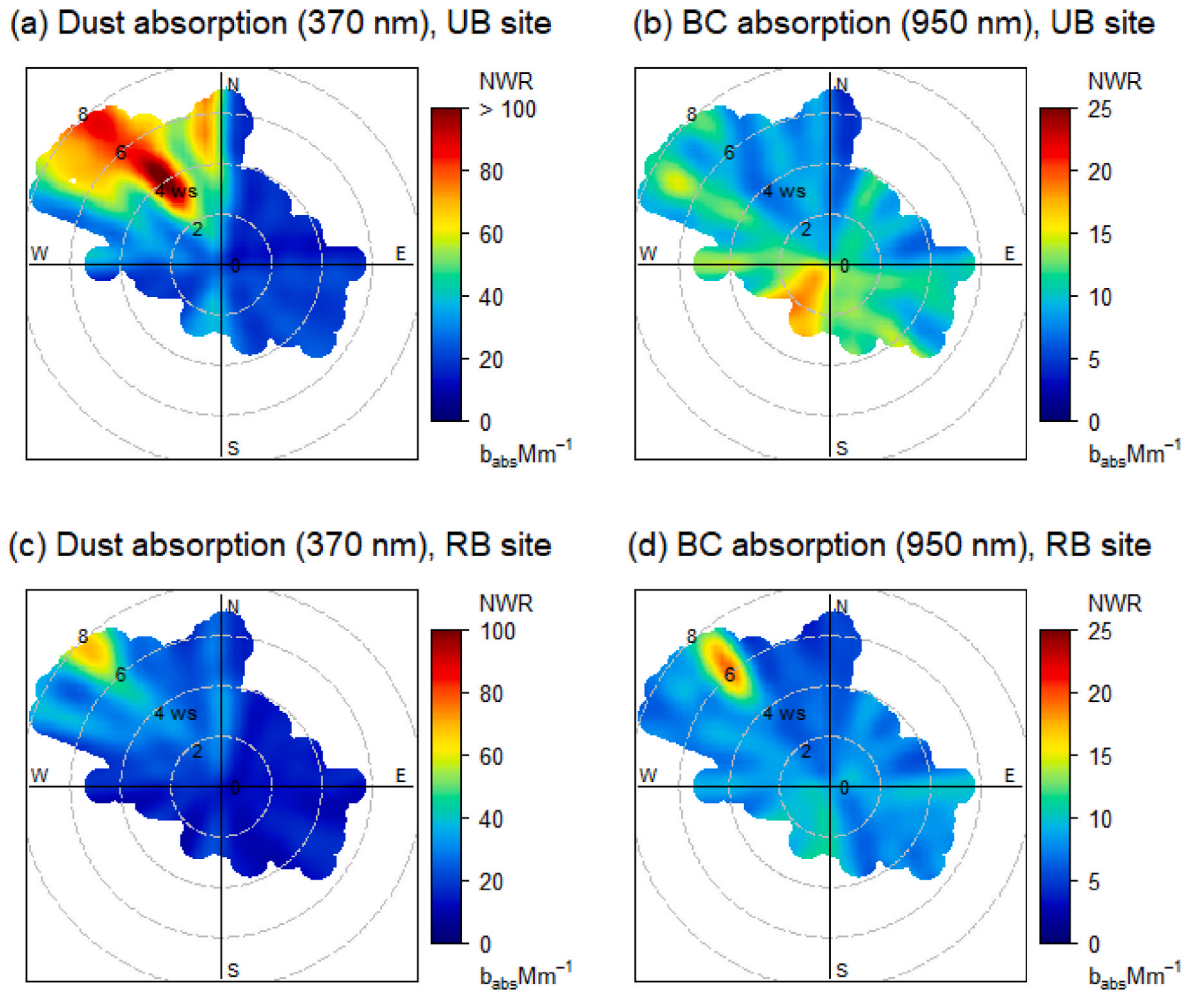

Fig. 10. NWR plots of dust (a, c) and BC-dominated (b, d) aerosols absorption at the UB and RB sites, respectively. Note: different absorption (Mm^{-1}) scales are used.

typical diurnal variations, peaking in the morning hours at both locations. The absence of a significant difference in AAE (370/950 nm) for dust between the UB (1.76 ± 0.26) and RB (1.87 ± 0.26) sites during NonDS periods suggests similar mechanisms of dust resuspension, mixing with other aerosols, and composition. However, dust storms led to an increase in AAE for dust to 2.16 ± 0.08 (UB) and 2.14 ± 0.06 (RB), indicating contamination of dust with BC during DS periods. BC AAE (370/950) showed similar means during both DS and NonDS periods, with values of 0.97 ± 0.2 (UB) and 0.95 ± 0.2 (RB) for DS, and 1.11 ± 0.2 (UB) and 1.10 ± 0.3 (RB) for NonDS.

The results from the NWR and PSCF analyses agree regarding the potential sources of desert dust and BC aerosol components. The significant contribution of long-range dust at both sites is associated with northwesterly winds. On the other hand, potential BC sources indicate a combination of local sources associated with southern winds and regional sources related to northwesterly, northeasterly, and easterly winds, which may be attributed to transboundary anthropogenic emissions. The high probability of potential local BC sources, identified with a southwesterly wind at the UB site, may lead to urban-related influences extending downwind towards the RB site.

Financial support

This research was supported by the project Detection of non-anthropogenic air pollution (DNAAP), the Slovenian Research Agency (Javna Agencija za Raziskovalno Dejavnost RS programmes P1-0188 and P1-0385), Helmholtz European Partnering (CROSSING project, Grant No: PIE-0007) and the European Union's Horizon 2020 research and innovation programme ("RADIATE", Grant No. 824096).

CRediT authorship contribution statement

Mohamed M.K. Mahfouz: Conceptualization, Data curation, Methodology, Visualization, Writing – original draft. **Gregor Skok:** Conceptualization, Validation, Visualization, Writing – review & editing. **Jean Sciare:** Conceptualization, Formal analysis, Writing – review & editing. **Michael Pikridas:** Conceptualization, Methodology, Validation, Writing – review & editing. **M. Rami Alfarra:** Methodology. **Shamjad Moosakutty:** Methodology, Writing – review & editing. **Balint Alfoldy:** Conceptualization, Project administration, Validation, Writing – original draft, Writing – review & editing. **Matic Ivančič:** Conceptualization, Investigation, Methodology, Project administration, Validation, Visualization, Writing – review & editing. **Martin Rigler:** Project administration, Writing – review & editing. **Asta Gregorič:** Conceptualization, Methodology, Project administration, Validation, Writing – review & editing. **Rok Podlipec:** Formal analysis, Visualization, Conceptualization. **Svenja Lohmann:** Formal analysis, Visualization. **Gregor Hlawacek:** Formal analysis, Visualization. **Rene Heller:** Formal analysis, Visualization. **Ersin Tutsak:** Conceptualization, Data curation, Methodology, Validation, Writing – review & editing. **Griša Močnik:** Conceptualization, Investigation, Methodology, Project administration, Supervision, Validation, Writing – review & editing.

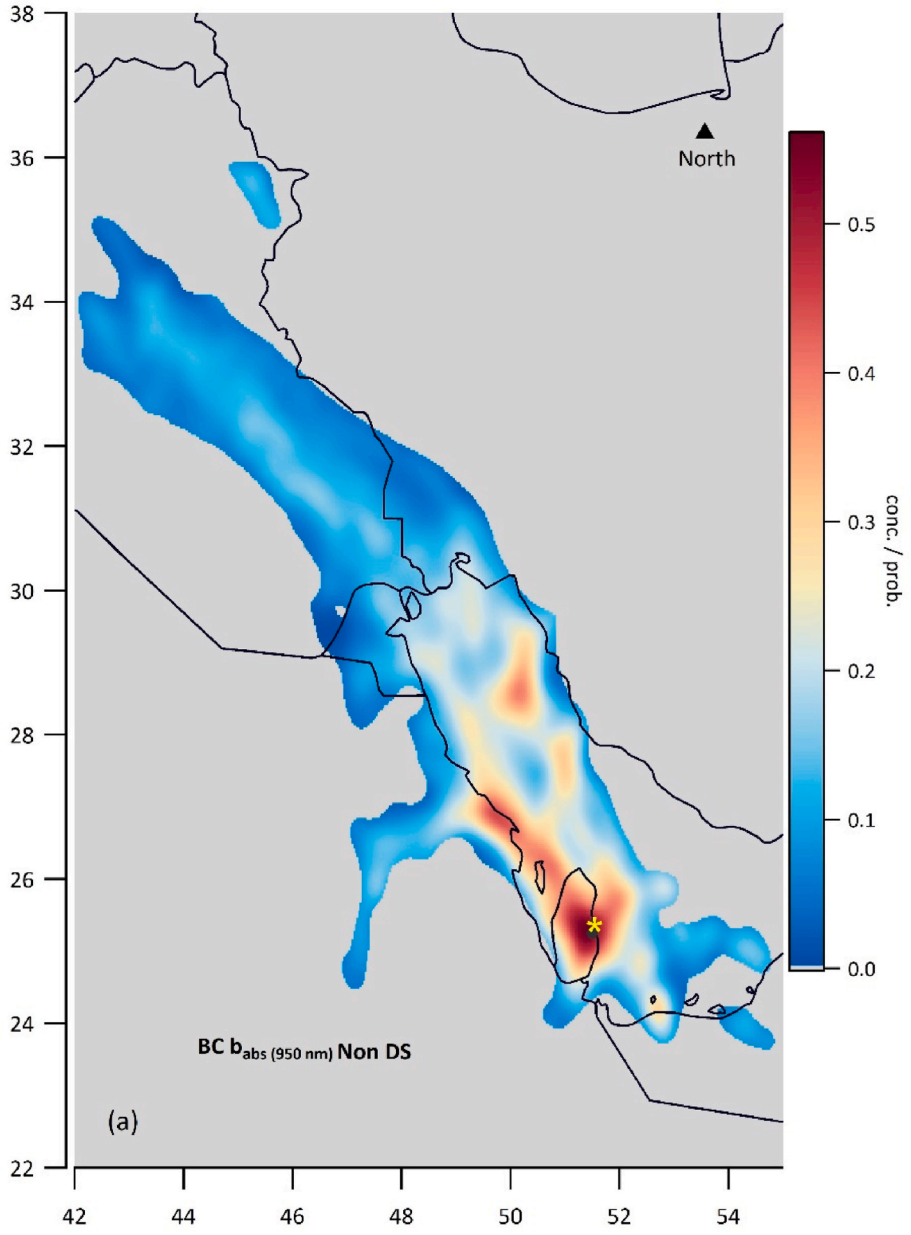

Fig. 11. PSCF plot for BC absorption at 950 nm during NonDS periods at the UB site.

Declaration of generative AI and AI-assisted technologies in the writing process

During the preparation of this work the authors used ChatGPT v3.5 in order to improve the English language in some parts of the manuscript. After using this tool/service, the authors reviewed and edited the content as needed and take full responsibility for the content of the publication.

Declaration of competing interest

The authors declare the following financial interests/personal relationships which may be considered as potential competing interests:

The coauthors BA, AG, MR and MI are employed by the manufacturer of instruments used in the study. The coauthor GM is employed part-time by the manufacturer of aerosol instruments. If there are other authors, they declare that they have no known competing financial interests or personal relationships that could have appeared to influence the work reported in this paper. If there are other authors, they declare that they have no known competing financial interests or personal relationships that could have appeared to influence the work reported in this paper.

Data availability

Data will be made available on request.

6 Acknowledgments

The authors acknowledge the ESC laboratories staff and the Cyprus Institute for their efforts and support during the project. Thanks are also due to Dr Edward Chatting and Murray James Bales for a thorough review of the manuscript and language editing.

Appendix A. Supplementary data

Supplementary data to this article can be found online at https://doi.org/10.1016/j.atmosenv.2024.120427.

References

Aerosol Magee Scientific, 2018. Aethalometer Model AE33 User Manual, 1.57 (Issue January).

Al-Dousari, A.M., Al-Awadhi, J., 2012. Dust fallout in northern Kuwait, major sources and characteristics. Kuwait J. Sci. Eng. 39 (2 A), 171–187.

Alfaro, S.C., Lafon, S., Rajot, J.L., Formenti, P., Gaudichet, A., Maillé, M., 2004. Iron oxides and light absorption by pure desert dust: an experimental study. J. Geophys. Res. Atmos. 109 (8), 1–9. https://doi.org/10.1029/2003JD004374.

Alfoldy, B., Mahfouz, M.M., Gregoric, A., Ivancic, M., Jezek, I., Rigler, M., 2021. Atmospheric concentrations and emission ratios of black carbon and nitrogen oxides in the Arabian/Persian Gulf region atmospheric concentrations and emission ratios of black carbon and nitrogen oxides in the Arabian/Persian Gulf region. Atmos. Environ. 256 (June) https://doi.org/10.1016/j.atmosenv.2021.118451.

American Meteorological Society, 2022. Streamline. https://glossary.ametsoc.org/wiki/.

Arnott, W.P., Hamasha, K., Moosmüller, H., Sheridan, P.J., Ogren, J.A., 2005. Towards aerosol light-absorption measurements with a 7-wavelength aethalometer: evaluation with a photoacoustic instrument and 3-wavelength nephelometer. Aerosol. Sci. Technol. 39 (1), 17–29. https://doi.org/10.1080/027868290901972.

Bachmann, J., 2009. Black Carbon: A Science/Policy Primer, vol. 45. December. http://www.c2es.org/docUploads/black-carbon-12-16-09.pdf.

Baumgardner, D., Avallone, L., Bansemer, A., Borrmann, S., Brown, P., Bundke, U., Chuang, P.Y., Cziczo, D., Field, P., Gallagher, M., Gayet, J.-F., Heymsfield, A., Korolev, A., Krämer, M., McFarquhar, G., Mertes, S., Möhler, O., Lance, S., Lawson, P., et al., 2012. In situ, airborne instrumentation: addressing and solving measurement problems in ice clouds. Bull. Am. Meteorol. Soc. 93 (2), ES29–ES34. https://doi.org/10.1175/BAMS-D-11-00123.1.

Bond, T.C., Doherty, S.J., Fahey, D.W., Forster, P.M., Berntsen, T., Deangelo, B.J., Flanner, M.G., Ghan, S., Kärcher, B., Koch, D., Kinne, S., Kondo, Y., Quinn, P.K., Sarofim, M.C., Schultz, M.G., Schulz, M., Venkataraman, C., Zhang, H., Zhang, S., et al., 2013. Bounding the role of black carbon in the climate system: a scientific assessment. J. Geophys. Res. Atmos. 118 (11), 5380–5552. https://doi.org/10.1002/jgrd.50171.

Bond, Tami C., Covert, D.S., Muller, T., 2009. Truncation and angular-scattering corrections for absorbing aerosol in the TSI 3563 nephelometer. Aerosol. Sci. Technol. 43 (9), 866–871. https://doi.org/10.1080/02786820902998373.

Bond, Tami C., Bergstrom, R.W., 2006. Light absorption by carbonaceous particles : an investigative review light absorption by carbonaceous particles : an investigative review. Aerosol. Sci. Technol. 40, 27–67. https://doi.org/10.1080/02786820500421521.

Cappa, C.D., Kolesar, K.R., Zhang, X., Atkinson, D.B., Pekour, M.S., Zaveri, R.A., Zelenyuk, A., Zhang, Q., 2016. Understanding the optical properties of ambient sub- and supermicron particulate matter: results from the CARES 2010 field study in northern California. Atmos. Chem. Phys. 16 (10), 6511–6535. https://doi.org/10.5194/acp-16-6511-2016.

Carslaw, D.C., Ropkins, K., 2012. Openair — an R package for air quality data analysis. Environ. Model. Software 27–28, 52–61. https://doi.org/10.1016/j.envsoft.2011.09.008.

Cheng, M.-D., Hopke, P.K., Zeng, Y., 1993. A receptor-oriented methodology for determining source regions of particulate sulfate observed at Dorset, Ontario. J. Geophys. Res. Atmos. 98 (D9), 16839–16849. https://doi.org/10.1029/92JD02622.

Clarke, A.D., Shinozuka, Y., Kapustin, V.N., Howell, S., Huebert, B., Doherty, S., Anderson, T., Covert, D., Anderson, J., Hua, X., Moore, K.G., McNaughton, C., Carmichael, G., Weber, R., 2004. Size distributions and mixtures of dust and black carbon aerosol in Asian outflow: physiochemistry and optical properties. J. Geophys. Res. Atmos. 109 (15), 1–20. https://doi.org/10.1029/2003JD004378.

Coen, M.C., Weingartner, E., Apituley, A., Ceburnis, D., Flentje, H., Henzing, J.S., 2010. Minimizing light absorption measurement artifacts of the Aethalometer : evaluation of five correction algorithms. Atmos. Meas. Tech. 3, 457–474.

Coen, M.C., Weingartner, E., Schaub, D., Hueglin, C., Corrigan, C., Henning, S., Schwikowski, M., 2004. Shaaran dust events at the Jungfraujoch detection by wavelength deenden of the single scattering albedo, vol. 1986, 2465–2480.

Comer, B., Olmer, N., Mao, X., Roy, B., Rutherford, D., 2017. Black Carbon Emissions and Fuel Use in 2015. International Council on Clean Transportation (ICCT).

Costabile, F., Barnaba, F., Angelini, F., Gobbi, G.P., 2013. Identification of key aerosol populations through their size and composition resolved spectral scattering and absorption. Atmos. Chem. Phys. 13 (5), 2455–2470. https://doi.org/10.5194/acp-13-2455-2013.

Denier van der Gon, H., Jozwicka, M., Hendriks, E., Gondwe, M., Schaap, M., 2010. Mineral Dust as a Component of Particulate Matter. PBL Netherlands Environmental Assesment Agency, p. 160. https://www.pbl.nl/en/publications/Mineral-Dust-component-particulate-matter.

Di Biagio, C., Formenti, P., Balkanski, Y., Caponi, L., Cazaunau, M., Pangui, E., Journet, E., Nowak, S., Andreae, M., Kandler, K., Saeed, T., Piketh, S., Seibert, D., Williams, E., Doussin, J.-F., 2019. Complex refractive indices and single scattering albedo of global dust aerosols in the shortwave spectrum and relationship to iron content and size. Complex Refractive Indices and Single Scattering Albedo of Global Dust Aerosols in the Shortwave Spectrum and Relationship to Iron Content and Size 1–42. https://doi.org/10.5194/acp-2019-145.

Di Biagio, C., Formenti, P., Cazaunau, M., Pangui, E., Marchand, N., Doussin, J.-F., 2017. Aethalometer multiple scattering correction Cref for mineral dust aerosols. Atmos. Meas. Tech. 10 (8), 2923–2939. https://amt.copernicus.org/articles/10/2923/2017/.

Diapouli, E., Popovicheva, O., Kistler, M., Vratolis, S., Persiantseva, N., Timofeev, M., Kasper-Giebl, A., Eleftheriadis, K., 2014. Physicochemical characterization of aged biomass burning aerosol after long-range transport to Greece from large scale wildfires in Russia and surrounding regions, Summer 2010. Atmos. Environ. 96, 393–404. https://doi.org/10.1016/j.atmosenv.2014.07.055.

Draxler, R., 2018. HYSPLIT4 User ' S Guide HYSPLIT4 USER ' S GUIDE. February.

Drinovec, L., Gregori, A., Zotter, P., Wolf, R., Bruns, E.A., Prévôt, A.S.H., Petit, J.-E., Favez, O., Sciare, J., Arnold, I.J., Chakrabarty, R.K., Moosmüller, H., Filep, A., MocnikLuka, G., 2017. The Filter-Loading Effect by Ambient Aerosols in Filter Absorption Photometers Depends on the Coating of the Sampled Particles, pp. 1043–1059. https://doi.org/10.5194/amt-10-1043-2017.

Drinovec, L., Sciare, J., Stavroulas, I., Bezantakos, S., Pikridas, M., Unga, F., Savvides, C., Višić, B., Remškar, M., Mocnik, G., 2020. A new optical-based technique for real-time measurements of mineral dust concentration in PM10 using a virtual impactor. Atmos. Meas. Tech. 13 (7), 3799–3813. https://doi.org/10.5194/amt-13-3799-2020.

Drinovec, Mocnik, G., Zotter, P., Prévôt, A.S.H.H., Ruckstuhl, C., Coz, E., Rupakheti, M., Sciare, J., Müller, T., Wiedensohler, A., Hansen, A.D.A.A., 2015. The "dual-spot" Aethalometer: an improved measurement of aerosol black carbon with real-time loading compensation. Atmos. Meas. Tech. 8 (5), 1965–1979. https://doi.org/10.5194/amt-8-1965-2015.

Dubovik, O., Holben, B., Eck, T.F., Smirnov, A., Kaufman, Y.J., King, M.D., Tanré, D., Slutsker, I., 2002. Variability of absorption and optical properties of key aerosol types observed in worldwide locations. J. Atmos. Sci. 59 (3), 590–608. https://doi.org/10.1175/1520-0469(2002)059%3C0590%3AVOAAOP%3E2.0.C.

Ealo, M., Alastuey, A., Ripoll, A., Pérez, N., Minguillón, M.C., Querol, X., Pandolfi, M., 2016. Detection of Saharan dust and biomass burning events using near-real-time intensive aerosol optical properties in the north-western Mediterranean. Atmos. Chem. Phys. 16 (19), 12567–12586. https://doi.org/10.5194/acp-16-12567-2016.

El-Baz, Farouk, Makharita, R.M., 2016. The Gulf War and the Environment. Routledge. https://www.taylorfrancis.com/books/mono/10.4324/9781315621418/gulf-war-environment-farouk-el-baz-makharita.

Fialho, P., Cerqueira, M., Pio, C., Cardoso, J., Nunes, T., Custódio, D., Alves, C., Almeida, S.M., Almeida-Silva, M., Reis, M., Rocha, F., 2014. The application of a multi-wavelength aethalometer to estimate iron dust and black carbon concentrations in the marine boundary layer of Cape Verde. Atmos. Environ. 97, 136–143. https://doi.org/10.1016/j.atmosenv.2014.08.008.

Fialho, P., Hansen, A.D.A., Honrath, R.E., 2005. Absorption coefficients by aerosols in remote areas: a new approach to decouple dust and black carbon absorption coefficients using seven-wavelength Aethalometer data. J. Aerosol Sci. 36 (2), 267–282. https://doi.org/10.1016/j.jaerosci.2004.09.004.

Hansen, A.D.A., Rosen, H., Novakov, T., 1982. Real-time measurement of the absorption coefficient of aerosol particles. Appl. Opt. 21 (17), 3060–3062. https://doi.org/10.1364/AO.21.003060.

Hansen, A.D.A., Rosen, H., Novakov, T., 1984. The aethalometer — an instrument for the real-time measurement of optical absorption by aerosol particles. Sci. Total Environ. 36, 191–196. https://doi.org/10.1016/0048-9697(84)90265-1.

Henry, R., Norris, G.a., Vedantham, R., Turner, J.R., 2009. Source region identification using kernel smoothing. Environ. Sci. Technol. 43 (11), 4090–4097.

Hersbach, H., Bell, B., Berrisford, P., Hirahara, S., Horányi, A., Muñoz-Sabater, J., Nicolas, J., Peubey, C., Radu, R., Schepers, D., Simmons, A., Soci, C., Abdalla, S., Abellan, X., Balsamo, G., Bechtold, P., Biavati, G., Bidlot, J., Bonavita, M., et al., 2020. The ERA5 global reanalysis. Q. J. R. Meteorol. Soc. 146 (730), 1999–2049. https://doi.org/10.1002/qj.3803.

Hess, M., Koepke, P., Schult, I., 1998. Optical properties of aerosols and clouds: the software package OPAC. Bull. Am. Meteorol. Soc. 79 (5), 831–844. https://doi.org/10.1175/1520-0477(1998)079<0831:OPOAAC>2.0.CO;2.

Hlawacek, G., Veligura, V., van Gastel, R., Poelsema, B., 2014. Helium ion microscopy. J. Vac. Sci. Technol. B 32 (2), 20801. https://doi.org/10.1116/1.4863676.

IARC, P. 161, 2013. Air Pollution and Cancer. IARC SCIENTIFIC. https://doi.org/10.1007/978-3-319-62731-1_24. Issue 161.

IPCC, 2023. The earth's energy budget, climate feedbacks and climate sensitivity. In I. P. on C. C. (IPCC). In: Climate Change 2021 – the Physical Science Basis. Cambridge University Press, pp. 923–1054. https://doi.org/10.1017/9781009157896.009.

Izhar, S., Gupta, T., Panday, A.K., 2020. Improved method to apportion optical absorption by black and brown carbon under the influence of haze and fog at Lumbini, Nepal, on the Indo-Gangetic Plains. Environ. Pollut. 263, 114640 https://doi.org/10.1016/j.envpol.2020.114640.

Kalbermatter, D.M., Močnik, G., Drinovec, L., Visser, B., Röhrbein, J., Oscity, M., Weingartner, E., Hyvärinen, A.P., Vasilatou, K., 2022. Comparing black-carbon-and aerosol-absorption-measuring instruments-A new system using lab-generated soot coated with controlled amounts of secondary organic matter. Atmos. Meas. Tech. 15 (2), 561–572. https://doi.org/10.5194/amt-15-561-2022.

Kaskaoutis, D.G., Grivas, G., Stavroulas, I., Liakakou, E., Dumka, U.C., Dimitriou, K., Gerasopoulos, E., Mihalopoulos, N., 2021. In situ identification of aerosol types in Athens, Greece, based on long-term optical and on online chemical characterization. Atmos. Environ. 246 (October 2020), 118070 https://doi.org/10.1016/j.atmosenv.2020.118070.

Kirchstetter, T.W., Novakov, T., Hobbs, P.V., 2004. Evidence that the spectral dependence of light absorption by aerosols is affected by organic carbon. J. Geophys. Res. Atmos. 109 (21), 1–12. https://doi.org/10.1029/2004JD004999.
Lewandowska, A.U., Falkowska, L.M., 2013. Sea salt in aerosols over the southern Baltic. Part 1. The generation and transportation of marine particles. Oceanologia 55 (2), 279–298. https://doi.org/10.5697/oc.55-2.279.
Liu, Q., Huang, Z., Hu, Z., Dong, Q., Li, S., 2022. Long-range transport and evolution of saharan dust over east asia from 2007 to 2020. J. Geophys. Res. Atmos. 127 (18), 1–21. https://doi.org/10.1029/2022JD036974.
Massabò, D., Caponi, L., Bernardoni, V., Bove, M.C., Brotto, P., Calzolai, G., Cassola, F., Chiari, M., Fedi, M.E., Fermo, P., Giannoni, M., Lucarelli, F., Nava, S., Piazzalunga, A., Valli, G., Vecchi, R., Prati, P., 2015. Multi-wavelength optical determination of black and brown carbon in atmospheric aerosols. Atmos. Environ. 108, 1–12. https://doi.org/10.1016/j.atmosenv.2015.02.058.
Mbengue, S., Zikova, N., Schwarz, J., Vodička, P., Šmejkalová, A.H., Holoubek, I., 2021. Mass absorption cross-section and absorption enhancement from long term black and elemental carbon measurements: a rural background station in Central Europe. Sci. Total Environ. 794 https://doi.org/10.1016/j.scitotenv.2021.148365.
Moosmüller, H., Chakrabarty, R.K., Arnott, W.P., 2009. Aerosol light absorption and its measurement: a review. J. Quant. Spectrosc. Radiat. Transf. 110 (11), 844–878. https://doi.org/10.1016/j.jqsrt.2009.02.035.
Moosmüller, H., Chakrabarty, R.K., Ehlers, K.M., Arnott, W.P., 2011. Absorption Ångström coefficient, brown carbon, and aerosols: basic concepts, bulk matter, and spherical particles. Atmos. Chem. Phys. 11 (3), 1217–1225. https://doi.org/10.5194/acp-11-1217-2011.
Moosmüller, Hans, Engelbrecht, J.P., Skiba, M., Frey, G., Chakrabarty, R.K., Arnott, W.P., 2012. Single scattering albedo of fine mineral dust aerosols controlled by iron concentration. J. Geophys. Res. Atmos. 117 (11) https://doi.org/10.1029/2011JD016909.
Müller, T., Laborde, M., Kassell, G., Wiedensohler, A., 2011. Design and performance of a three-wavelength LED-based total scatter and backscatter integrating nephelometer. Atmos. Meas. Tech. 4 (6), 1291–1303. https://doi.org/10.5194/amt-4-1291-2011.
Müller, T., Paixão, M., Wiedensohler, A., 2012. Scattering coefficients and asymmetry parameters derived from the polar nephelometer Aurora4000. European Aerosol Conference 29 (7), 4000.
Nakayama, T., Zhao, W., Zhang, W., 2021. Measurements of aerosol optical properties using spectroscopic techniques. In: Chen, W., Venables, D.S., Sigrist, M.W. (Eds.), Advances in Spectroscopic Monitoring of the Atmosphere. Elsevier, pp. 345–412. https://doi.org/10.1016/B978-0-12-815014-6.00003-8.
Nara, H., Tanimoto, H., Tohjima, Y., Mukai, H., Nojiri, Y., Machida, T., 2014. Emissions of methane from offshore oil and gas platforms in Southeast Asia. Sci. Rep. 4 (April 2012), 1–6. https://doi.org/10.1038/srep06503.
NASA, 2022. Dust Storm over Iraq. EarthData. https://www.earthdata.nasa.gov/worldview/worldview-image-archive/dust-storm-over-iraq.
NOAA, 2019. Global Data Assimilation System (GDAS). https://www.ncdc.noaa.gov/data-access/model-data/model-datasets/global-data-assimilation-system-gdas.
Pandolfi, M., Cusack, M., Alastuey, A., Querol, X., 2011. Variability of aerosol optical properties in the western mediterranean basin. Atmos. Chem. Phys. 11 (15), 8189–8203. https://doi.org/10.5194/acp-11-8189-2011.
Peters, T.M., Ott, D., O'Shaughnessy, P.T., 2006. Comparison of the Grimm 1.108 and 1.109 portable aerosol spectrometer to the TSI 3321 aerodynamic particle sizer for dry particles. Ann. Occup. Hyg. 50 (8), 843–850. https://doi.org/10.1093/annhyg/mel067.
Petit, J.-E., Favez, O., Albinet, A., Canonaco, F., 2017a. A user-friendly tool for comprehensive evaluation of the geographical origins of atmospheric pollution : wind and trajectory analyses. Environ. Model. Software 88, 183–187. https://doi.org/10.1016/j.envsoft.2016.11.022.
Petit, J.E., Favez, O., Albinet, A., Canonaco, F., Sciare, J., Crenn, V., Sarda-Estève, R., Bonnaire, N., Močnik, G., Dupont, J.C., Haeffelin, M., Leoz-Garziandia, E., 2017b. A user-friendly tool for comprehensive evaluation of the geographical origins of atmospheric pollution: wind and trajectory analyses. Atmos. Chem. Phys. 88 (6), 183–187. https://doi.org/10.5194/acp-15-2985-2015.
Petzold, A., Rasp, K., Weinzierl, B., Esselborn, M., Hamburger, T., Dörnbrack, A., Kandler, K., Schütz, L., Knippertz, P., Fiebig, M., Virkkula, A., 2009. Saharan dust absorption and refractive index from aircraft-based observations during SAMUM 2006. Tellus Ser. B Chem. Phys. Meteorol. 61 (1), 118–130. https://doi.org/10.1111/j.1600-0889.2008.00383.x.
Reid, J.S., Jonsson, H.H., Maring, H.B., Smirnov, A., Savoie, D.L., Cliff, S.S., Reid, E.A., Livingston, J.M., Meier, M.M., Dubovik, O., Tsay, S.C., 2003. Comparison of size and morphological measurements of coarse mode dust particles from Africa. J. Geophys. Res. Atmos. 108 (19) https://doi.org/10.1029/2002jd002485.
Romano, S., Perrone, M.R., Pavese, G., Esposito, F., Calvello, M., 2019. Optical properties of PM2.5 particles: results from a monitoring campaign in southeastern Italy. Atmos. Environ. 203 (June 2018), 35–47. https://doi.org/10.1016/j.atmosenv.2019.01.037.
Sandradewi, J., Prévôt, A.S.H.H., Szidat, S., Perron, N., Alfarra, M.R., Lanz, V.A., Weingartner, E., Baltensperger, U.R.S., 2008. Using aerosol light absorption measurements for the quantitative determination of wood burning and traffic emission contribution to particulate matter. Environ. Sci. Technol. 42 (9), 3316–3323. https://doi.org/10.1021/es702253m.
Schmeisser, L., Andrews, E., Ogren, J.A., Sheridan, P., Jefferson, A., Sharma, S., Kim, J. E., Sherman, J.P., Sorribas, M., Kalapov, I., Arsov, T., Angelov, C., Mayol-Bracero, O. L., Labuschagne, C., Kim, S.-W.S.W., Hoffer, A., Lin, N.-H.N.H., Chia, H.P.H.-P., Bergin, M., et al., 2017. Classifying aerosol type using in situ surface spectral aerosol optical properties. Atmos. Chem. Phys. 17 (19), 12097–12120. https://doi.org/10.5194/acp-17-12097-2017.
Scipioni, L., Stern, L.A., Notte, J., Sijbrandij, S., Griffin, B., 2008. Helium ion microscope. Adv. Mater. Process. 166 (6), 27–30. https://doi.org/10.1201/9781420075250-c39.
Shamjad, P.M., Satish, R.V., Thamban, N.M., Rastogi, N., Tripathi, S.N., 2018. Absorbing refractive index and direct radiative forcing of atmospheric Brown carbon over gangetic plain. ACS Earth Space Chem. 2 (1), 31–37. https://doi.org/10.1021/acsearthspacechem.7b00074.
Sokolik, I.N., Toon, O.B., 1999. Incorporation of mineralogical composition into models of the radiative properties of mineral aerosol from UV to IR wavelengths. J. Geophys. Res. Atmos. 104 (D8), 9423–9444. https://doi.org/10.1029/1998JD200048.
Tanaka, T.Y., Chiba, M., 2006. A numerical study of the contributions of dust source regions to the global dust budget. Global Planet. Change 52 (1), 88–104. https://doi.org/10.1016/j.gloplacha.2006.02.002.
Teri, M., Müller, T., Gasteiger, J., Valentini, S., Horvath, H., Vecchi, R., Bauer, P., Walser, A., Weinzierl, B., 2021. Impact of Particle Size , Refractive Index , and Shape on the Determination of the Particle Scattering Coefficient - an Optical Closure Study Evaluating Different Nephelometer Angular Truncation and Illumination Corrections, pp. 1–41. December.
Tohidi, R., Farahani, V.J., Sioutas, C., 2022. Real-time measurements of mineral dust concentration in coarse particulate matter (PM10–2.5) by employing a novel optical-based technique in Los Angeles. Sci. Total Environ. 838 (February), 156215 https://doi.org/10.1016/j.scitotenv.2022.156215.
TSI Inc, 2022. Optical Particle Sizer Proven Technology for Highly Resolved Particle Sizing chrome-extension://efaidnbmnnnibpcajpcglclefindmkaj/https://tsi.com/getmedia/9728dd3d-5528-4621-9877-a116ee742528/3330_5001323_Web?ext=.pdf.
Valentini, S., Barnaba, F., Bernardoni, V., Calzolai, G., Costabile, F., Di Liberto, L., Forello, A.C., Gobbi, G.P., Gualtieri, M., Lucarelli, F., Nava, S., Petralia, E., Valli, G., Wiedensohler, A., Vecchi, R., 2020. Classifying aerosol particles through the combination of optical and physical-chemical properties: results from a wintertime campaign in Rome (Italy). Atmos. Res. 235 (August 2019), 104799 https://doi.org/10.1016/j.atmosres.2019.104799.
Valenzuela, A., Olmo, F.J., Lyamani, H., Antón, M., Titos, G., Cazorla, A., Alados-Arboledas, L., 2015. Aerosol scattering and absorption Angström exponents as indicators of dust and dust-free days over Granada (Spain). Atmos. Res. 154, 1–13. https://doi.org/10.1016/j.atmosres.2014.10.015.
Villasenor, R., Magdaleno, M., Quintanar, A., Gallardo, J.C., López, M.T., Jurado, R., Miranda, A., Aguilar, M., Melgarejo, L.A., Palmerín, E., Vallejo, C.J., Barchet, W.R., 2003. An air quality emission inventory of offshore operations for the exploration and production of petroleum by the Mexican oil industry. Atmos. Environ. 37 (26), 3713–3729. https://doi.org/10.1016/S1352-2310(03)00445-X.
Weingartner, E., Saathoff, H., Schnaiter, M., Streit, N., Bitnar, B., Baltensperger, U., 2003. Absorption of light by soot particles: determination of the absorption coefficient by means of aethalometers. J. Aerosol Sci. 34 (10), 1445–1463. https://doi.org/10.1016/S0021-8502(03)00359-8.
Yang, M., Howell, S.G., Zhuang, J., Huebert, B.J., 2009. Attribution of aerosol light absorption to black carbon, brown carbon, and dust in China - interpretations of atmospheric measurements during EAST-AIRE. Atmos. Chem. Phys. 9 (6), 2035–2050. https://doi.org/10.5194/acp-9-2035-2009.
Yigiterhan, O., Alfoldy, B.Z., Giamberini, M., Turner, J.C., Al-Ansari, E.S., Abdel-Moati, M.A., Al-Maslamani, I.A., Kotb, M.M., Elobaid, E.A., Hassan, H.M., Obbard, J. P., Murray, J.W., 2018. Geochemical composition of Aeolian dust and surface deposits from the Qatar Peninsula. Chem. Geol. 476 (2018), 24–45. https://doi.org/10.1016/j.chemgeo.2017.10.030.
Yus-Díez, J., Via, M., Alastuey, A., Karanasiou, A., Minguillón, M.C., Perez, N., Querol, X., Reche, C., Ivančič, M., Rigler, M., Pandolfi, M., 2022. Absorption enhancement of black carbon particles in a Mediterranean city and countryside: effect of particulate matter chemistry, ageing and trend analysis. Atmos. Chem. Phys. 22 (13), 8439–8456. https://doi.org/10.5194/acp-22-8439-2022.
Yuval, Levi, Y., Dayan, U., Levy, I., Broday, D.M., 2020. On the association between characteristics of the atmospheric boundary layer and air pollution concentrations. Atmos. Res. 231, 104675 https://doi.org/10.1016/j.atmosres.2019.104675.

Zhang, X.Y., Wang, Y.Q., Niu, T., Zhang, X.C., Gong, S.L., Zhang, Y.M., Sun, J.Y., 2012. Atmospheric aerosol compositions in China: spatial/temporal variability, chemical signature, regional haze distribution and comparisons with global aerosols. Atmos. Chem. Phys. 12 (2), 779–799. https://doi.org/10.5194/acp-12-779-2012.

Zhao, Z., Cao, J., Chow, J.C., Watson, J.G., Chen, A.L.-W., Wang, X., Wang, Q., Tian, J., Shen, Z., Zhu, C., Liu, S., Tao, J., Ye, Z., Zhang, T., Zhou, J., Tian, R., 2019. Multi-wavelength light absorption of black and brown carbon at a high-altitude site on the Southeastern margin of the Tibetan Plateau, China. Atmos. Environ. 212, 54–64. https://doi.org/10.1016/j.atmosenv.2019.05.035.

Zhou, X., Zhou, T., Fang, S., Han, B., He, Q., 2023. Investigation of the vertical distribution characteristics and microphysical properties of summer mineral dust masses over the taklimakan desert using an unmanned aerial vehicle. Rem. Sens. 15 (14) https://doi.org/10.3390/rs15143556.

Zotter, P., Herich, H., Gysel, M., El-Haddad, I., Zhang, Y., Mocnik, G., Hüglin, C., Baltensperger, U., Szidat, S., Prévôt, A.S.H., 2017. Evaluation of the absorption Ångström exponents for traffic and wood burning in the Aethalometer-based source apportionment using radiocarbon measurements of ambient aerosol. Atmos. Chem. Phys. 17 (6), 4229–4249. https://doi.org/10.5194/acp-17-4229-2017.